Kidney Stones in μ-Reactors

Design/production of microfluidic devices for induction time experiments and a comparison between laboratory and micro scale reactors

Tsun Wang Yu

Technische Universiteit Delft

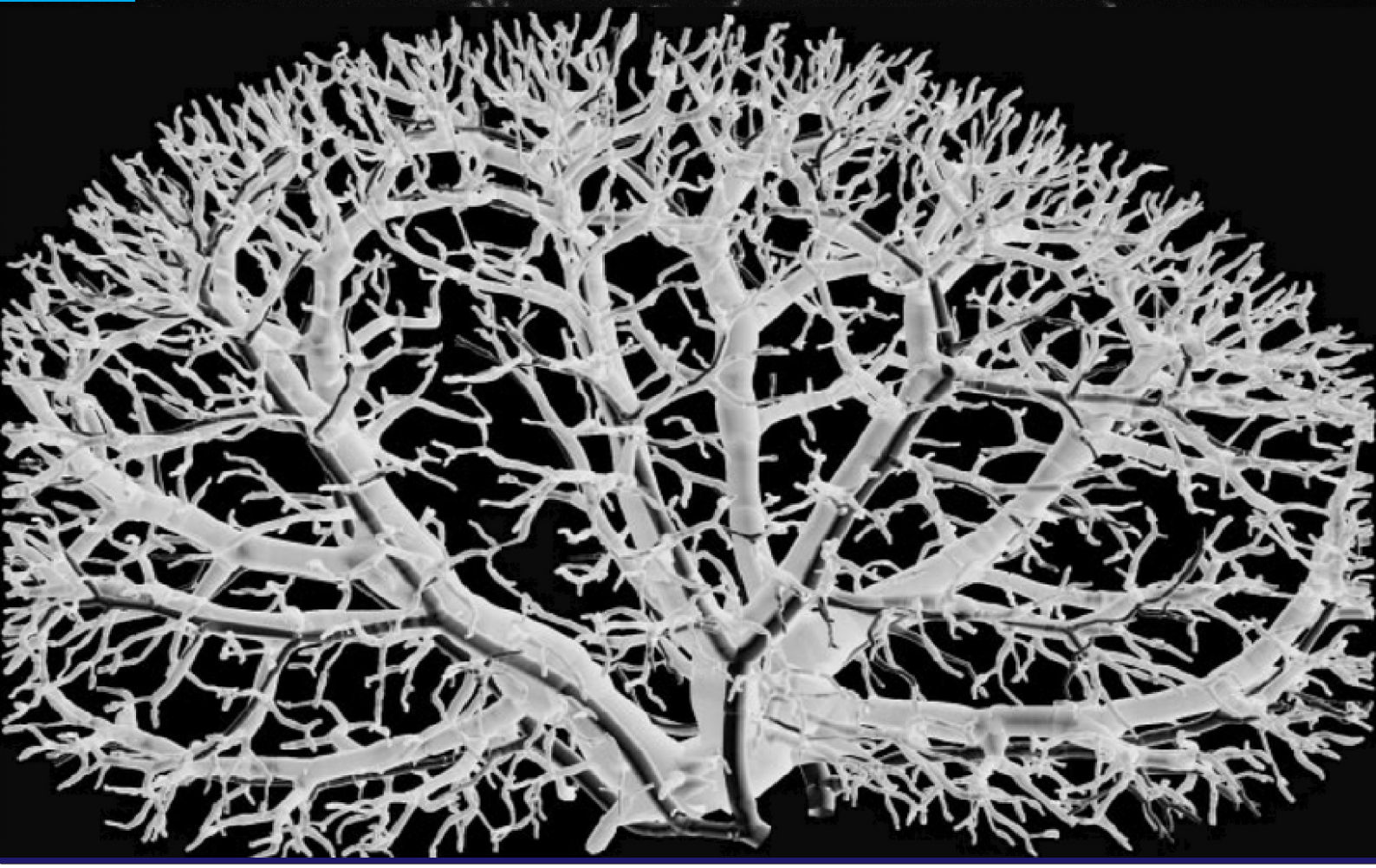

TU Delft Delft University of Technology

Challenge the future

KIDNEY STONES IN μ-REACTORS

DESIGN/PRODUCTION OF MICROFLUIDIC DEVICES FOR INDUCTION TIME EXPERIMENTS AND A COMPARISON BETWEEN LABORATORY AND MICRO SCALE REACTORS

by

Tsun Wang Yu
4325656

in partial fulfillment of the requirements for the degree of

Master of Science
in Chemical Engineering

at the Delft University of Technology,
to be defended publicly on Thursday November 21, 2019 at 11:00 AM.

Under guidance and supervision of:	Dr. H. B. Eral,	TU Delft
	MSc. F. İbiş,	TU Delft
Thesis committee:	Dr. H. B. Eral,	TU Delft
	Prof. Dr. A. E. D. M. van der Heijden,	TU Delft
	Prof. Ir. J. Grievink,	TU Delft

Report number: P&E-2887

TU Delft Delft University of Technology

ABSTRACT

Kidney stones disease is a serious healthy issue in modern society. The amount of patients getting kidney stones are increasing every year [1]. This trend can be caused my numerous reasons like dietary and living conditions. The main point is that the number of kidney stone disease patients need to be lowered. The first step to achieve this is by getting a better understanding of the process of kidney stone formation. The focus will be on calcium oxalate which is the main constituent of kidney stones.

In this study we present a microfluidic method to quantify nucleation kinetics of calcium oxalate as function of supersaturation, pH and in the presence of inhibitors (Magnesium (Mg^{2+}), Osteopontin).

We have optimized the design of the microfluidic device to minimize the droplet coalescence. Kinetic parameters were obtained through fitting of the probability of nucleation curves measured for over a hundred microdroplets.

Nucleation kinetics was seen to increase with an increase in supersaturation, as expected. At pH 6.0 the kinetics dramatically slows down compared to pH's 3.6 and 8.6. As the inhibitor concentration increases the kinetics will decrease, this is the case for both Mg^{2+} and Osteopontin.

ACKNOWLEDGEMENTS

First of all I want to thank **Dr. Burak Eral** and **MSc. Fatma İbiş** For their guidance. Without their guidance and feedback it would not have been possible to finish this thesis with great results as written in this report. When i chose this project group to do my thesis at, I was expecting a group with a great working environment and a place were I can learn a lot. But after working in this group for so many months, I can say that it has exceeded my expectations. I enjoyed my time here and had a lot of fun working with everyone in the department. All of this would not have been possible if i did not get the chance to work here from **Dr. Burak Eral** and **MSc. Fatma İbiş**, that is why i want to thank my supervisor and daily supervisor once more.

I also want to thank **Dr. Ir. Herman Kramer**, **Prof. Dr. Antoine van der Heijden** and **Dr. Ir. Frederico Marques Penha** for their guidance and input at all the weekly progress meetings. I was always looking forward to present good results to both of them.

I want to thank **Michel van den Brink** and **Jaap van Raamt** for helping me in and around the lab. Without their help my experiments would not have gone this smoothly.

The next group of people I want to thank are the people in the **PME department**. They were so kind to let me use their equipment such as the 3D printers and the spincoater. Also a special thanks to the **technicians of the PME department** who not only taught me how to use the 3D printers, but also helped me with all my questions that I had and problems that I faced.

It has been a great pleasure working with **Sanan Suleymanli**, **Monica Schneider**, **Rick Sluimer**, **Priya Dhand**, **Debadrita Ganguly**, **Jiali Wang** and **Mai Fujino** who were in the same project group as me. With some I have been working more than others, but the time spent with each of you were equally important to me.

I want to thank everyone individually but that is not possible that is why I want to thank **everyone else from the P&E department** who I have worked with or have helped me with my thesis. You all are just as important as the people mentioned above and I am very thankful.

I cannot end this acknowledgement without thanking my friends who would always find ways to cheer me up when I was down from all the hard work. They were the people who would keep me sane in this busy period where I was pushing myself to the limits. So thank you **Amira Anthonijsz**  , **Assia Aouichi**, **Djalil Salaheddine**, **Priya Dhand** and **Cas van Rijn** for being there when I had my ups and downs.

As last, I want to thank **my family** for always believing in me even when I did not believe I could do it myself. They were the driving force and there are no words that can describe the amount of gratitude and love I have for them.

Tsun Wang Yu
Delft, November 2019

List of Figures

1.1 Kidney anatomy[3] . . . 1
1.2 Different locations in the kidney where kidney stones can be found[5] . . . 2
1.3 Different kinds of calcium oxalate hydrates[10] . . . 3
1.4 ESWL schematic[8] . . . 3

2.1 Solubility diagram . . . 5
2.2 A schematic plot of gibbs free energy versus the radius of clusters[18] . . . 7
2.3 Schematic of the gibbs free energy over cluster radius for heterogeneous and homogeneous nucleation[18] . . . 7
2.4 Schematic of heterogeneous nucleation[18] . . . 8
2.5 Schematic of the FBRM probe [24] . . . 10
2.6 Schematic FBRM setup[27] . . . 11
2.7 Probability curves at different supersaturation ratio fitted with the exponential model . . . 12
2.8 Probability curves at different supersaturation ratios fitted with the Weibull model . . . 13
2.9 Logarithmic plot of J/S versus S to obtain the kinetic and thermodynamic parameters . . . 14

3.1 Schematic of a DLP printer [29] . . . 16
3.2 Envisiontec optical resin curing 3D printer [30] . . . 16
3.3 Curing machine for 3D printed objects [31] . . . 16
3.4 Droplet formation inside a micro channel with a T junction, a. shows the junction in 3d b. shows how the droplets are formed[32] . . . 16
3.5 Mixing flow of droplets in microfluidic bends[33] . . . 17
3.6 Intensity of segregation versus number of bends[35] . . . 17
3.7 3D printer setup . . . 18
3.8 Process of spincoating . . . 19
3.9 Schematic of sticking process . . . 19
3.10 Defects in several places of the microfluidic device caused by the defects in the mould . . . 20
(a) Defect in outlet channel . . . 20
(b) Defect in outlet bend . . . 20
(c) Defect in channel bend . . . 20
(d) Defect in channel . . . 20
3.11 Schematic of printing at an angle . . . 20
3.12 First design Made by P. van Tooren . . . 21
3.13 Second design with 3 inlets and mixing at the beginning . . . 21
3.14 Bursting of the wall between channels . . . 21
3.15 Third design with bigger dimensions of the channels . . . 22
3.16 Air trapped in the inlet reservoirs . . . 22
3.17 Fourth design with smaller inlets . . . 22
3.18 Final design of the microfluidic mould . . . 22
3.19 Droplet position at 0 hours and after 6 hours . . . 23
3.20 Description of the final design of the microfluidic mould . . . 23

4.1 Fluctuations in flow rate of pressure pump compared to syringe pump [41] . . . 26
4.2 Schematic of the pressure pump setup [41] . . . 26
4.3 Schematic of the reservoir used by the pressure pump [41] . . . 26
4.4 Parallel polarizers (polarizer and analyzer are aligned) . . . 27
4.5 Crossed polarizers (polarizer and analyzer are misaligned) . . . 27
4.6 Schematic of the pressure pump setup . . . 29
4.7 Time lapse of crystal formation inside a droplet under polarized light microscopy . . . 30

4.8 Probability curves at different supersaturation ratio fitted with the Weibull model 31
4.9 Logarithmic plot of J/S versus S to obtain the kinetic and thermodynamic parameters 32
4.10 Probability curves at different pH fitted with the Weibull model 33
4.11 Probability curves at different Magnesium concentrations fitted with the Weibull model 34
4.12 Probability curves at different osteopontin concentrations fitted with the Weibull model 35

C.1 Solubility of calcium oxalate at different pH 49

List of Tables

1.1 Types of stones[8] . . . 2

2.1 Chemicals used in lab scale experiments . . . 10
2.2 Equipment used in lab scale experiments . . . 10
2.3 Amount of chemical needed to prepare the supersaturated solutions for lab scale experiments . . . 11
2.4 Parameters t_g and τ from exponential model fitted into the probability distribution at different supersaturation . . . 12
2.5 Parameters k and τ from exponential model fitted into the probability distribution at different supersaturation . . . 13
2.6 The calculated median nucleation time and nucleation rate for the 3 different supersaturation ratios . . . 13

3.1 Chemicals used in microfluidic device process . . . 18
3.2 Equipment used in microfluidic device process . . . 18

4.1 Chemicals used in microfluidic experiments . . . 27
4.2 Equipment used in microfluidic experiments . . . 27
4.3 Amount of chemical needed to prepare the supersaturated solutions for microfluidic experiments 28
4.4 Amount of chemicals needed to prepare the buffer solutions for pH experiments . . . 28
4.5 Amount of magnesium chloride needed to prepare the supersaturated solutions for inhibitor experiments . . . 28
4.6 Amount of sodium oxalate needed to prepare the supersaturated solutions for osteopontin inhibitor experiments . . . 28
4.7 Amount of stock solution needed to prepare the supersaturated solutions for inhibitor experiments . . . 29
4.8 Parameters k and τ from Weibull model fitted into the probability distribution at different supersaturation ratio . . . 32
4.9 The calculated median nucleation time and nucleation rate for the 3 different supersaturation ratios . . . 32
4.10 Parameters k and τ from Weibull model fitted into the probability distribution at different pH . . . 33
4.11 Parameters k and τ from Weibull model fitted into the probability distribution at different magnesium concentrations . . . 34
4.12 Parameters k and τ from Weibull model fitted into the probability distribution at different osteopontin concentrations . . . 35

B.1 Constants used for flow rate calculations . . . 47
B.2 Flow rate data used for dimensionless number calculation . . . 47

Contents

List of Figures vii

List of Tables ix

1 Introduction 1
- 1.1 Kidney . . . 1
- 1.2 Urolithiasis . . . 2
  - 1.2.1 Statistics of kidney stones . . . 2
  - 1.2.2 Calcium oxalate crystals . . . 3
  - 1.2.3 Treatment . . . 3
- 1.3 Thesis Objectives . . . 4

2 Laboratory-Scale Experiments 5
- 2.1 Theoretical background . . . 5
  - 2.1.1 Supersaturation . . . 5
  - 2.1.2 Nucleation . . . 6
  - 2.1.3 Growth . . . 8
  - 2.1.4 Agglomeration . . . 8
  - 2.1.5 Induction Time . . . 8
  - 2.1.6 Weibull . . . 9
  - 2.1.7 Focused beam reflectance measurement . . . 9
- 2.2 Materials and methods . . . 10
  - 2.2.1 Materials & Equipment . . . 10
  - 2.2.2 Solution Preparation . . . 10
  - 2.2.3 Experimental conditions . . . 10
- 2.3 Results & discussion . . . 12

3 Design and Production of Microfluidic Devices 15
- 3.1 Theoretical background . . . 15
  - 3.1.1 3D printer . . . 15
  - 3.1.2 Droplet Formation . . . 16
  - 3.1.3 droplet mixing . . . 17
- 3.2 Materials and methods . . . 18
  - 3.2.1 Materials & Equipment . . . 18
  - 3.2.2 3D Printing . . . 18
  - 3.2.3 Hydrophobization . . . 18
  - 3.2.4 PDMS Chip Fabrication . . . 19
  - 3.2.5 Spincoating and Semi-curing . . . 19
- 3.3 Results & discussion . . . 20
  - 3.3.1 printing process . . . 20
  - 3.3.2 Different designs . . . 21
  - 3.3.3 Final design . . . 22

4 Microfluidic Experiments 25
- 4.1 Theoretical background . . . 25
  - 4.1.1 Dimensionless Numbers . . . 25
  - 4.1.2 pressure pump . . . 26
  - 4.1.3 Polarized light microscopy . . . 26

4.2 Materials and methods . . . 27
4.2.1 Materials & Equipment . . . 27
4.2.2 Solution Preparation . . . 27
4.2.3 Oil Preparation . . . 29
4.2.4 Pressure pumps . . . 29
4.2.5 polarized light microscopy . . . 30
4.3 Results & discussion . . . 31
4.3.1 Dimensionless numbers . . . 31
4.3.2 Induction time at different supersaturation . . . 31
4.3.3 pH dependent induction time . . . 32
4.3.4 Inhibitors . . . 33

5 Conclusion **37**
5.1 Induction time . . . 37
5.1.1 Laboratory scale . . . 37
5.1.2 microfluidics . . . 37
5.1.3 Difference between the two scales . . . 37
5.2 Influence of pH . . . 37
5.3 Influence of inhibitors . . . 38
5.3.1 Magnesium . . . 38
5.3.2 Osteopontin . . . 38

6 Recommendation **39**

Bibliography **41**

A Matlab code **43**

B Flow rate calculations **47**

C Solubility curve **49**

1

INTRODUCTION

Crystallization is a process where solids are formed in a homogeneous solution or melt by organizing atoms or molecules into crystalline structures. The formation of crystals consist of 2 major steps. The first step is nucleation, in this step small nuclei are formed in supersaturated solvent. The second step is crystal growth, in this step crystals will grow in size by either merging with other crystals or growing on its own.

Crystallization is commonly used in the industry for purification or separation of products. Crystallization can be used on bulk chemicals, for example salts and fertilizers; high value-added products like pharmaceuticals; and chemicals that are difficult to separate. But crystallization does not only occur in industry and is not always favorable. In the human body, which can be seen as a biological factory, crystallization also happens. In the kidney these crystals can develop into stone if not flushed out of the body.

To get a better understanding of the mechanism of kidney stone formation, an in vitro model is made to evaluate calcium. When this mechanism is well understood, research can be conducted on how to prevent kidney stones from forming.

1.1. KIDNEY

Kidneys are a bilateral organs, which means that they are located at both sides of the human body. An adult human kidney has an average size of 12 centimeter and an average volume of 170 mililiters [2].

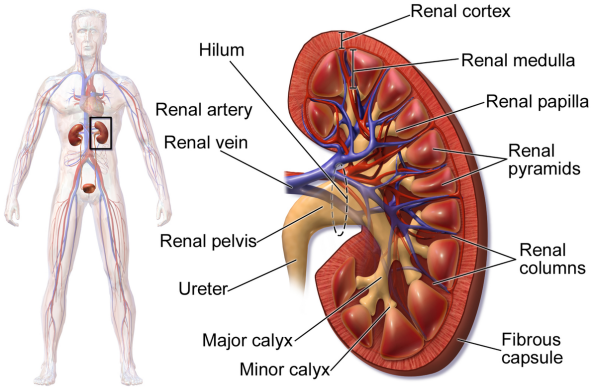

Figure 1.1: Kidney anatomy[3]

The kidneys are the filters of the body. They filter the blood to remove waste and keep bodily fluids in balance. Blood that needs to be filtered comes in from the renal artery and gets filtered in the nephrons. After filtering, the clean blood will exit from the renal vein and recirculate back into the body. All the waste that

has been filtered will leave the kidney from the collecting duct to the ureter and finally into the bladder as a concentrated liquid also known as urine. The urine can have a high concentration of ions such as calcium, oxalate and phosphate.

1.2. UROLITHIASIS

Urolithiasis is the scientific name for kidney stone disease. Kidney stone disease is a disease where a high concentration of ions crystallize and grow to a size which cannot pass through the renal ducts, ureter or urethra anymore. Some of the symptoms may include abdominal pain, lower back pain, blood in urine and painful urination [4]. When stones are discovered in a patients kidney, a suitable treatment will be decided depending on the size of the stones. Sizes up to 5 mm can pass through the urinary system naturally, while stones with a diameter of 5 to 7 mm has a 50% chance of passing through the body without medical attention [5]. Anything larger than that requires medical treatment to remove it from the body.

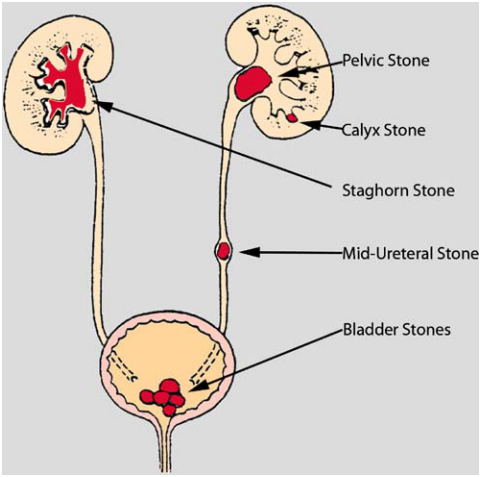

Figure 1.2: Different locations in the kidney where kidney stones can be found[5]

Kidney stones are devided into two different groups by shape, staghorn or non-staghorn. Staghorn stones are big stones that fills up multiple major and minor calices. Non-staghorn which can be described as calyceal, pelvic or ureteral depending on their location inside the kidney [5]. In figure 1.2 the ureter anatomy is shown with stones in the locations described above.

1.2.1. STATISTICS OF KIDNEY STONES

Kidney stone disease is a serious health problem that affect about 4% to 15% of the world population at some point in their lives [6]. The number of occurrences and recurrences are also increasing globally [1]. The recurrence rate is estimated to be 50% in the first 10 years and 75% in 20 years [4]. Suspected causes for these alarming trends are change in dietary and effects of global warming [7].

In the kidney, various types of stones can be found. But the most common stones are formed out of calcium oxalate, which has a frequency of occurence of 75% [8]. In table 1.1 the rest of the frequent stone types can be found.

Table 1.1: Types of stones[8]

Type	**Frequency (%)**	**Sex**
Calcium oxalate hydrates	75	M
Calcium phosphate (brushite)	5	F>M
Uric acid	5-15	M=F
Struvite (Mg ammonium phosphate)	10-20	F
Cystine	1	M=F

1.2.2. CALCIUM OXALATE CRYSTALS

As mentioned in the statistics of kidney stones, calcium oxalate is the most frequently found crystal type in kidney stones. But calcium oxalate also has different kinds of hydrates, mono-, di- and trihydrate. The most thermodynamically unstable hydrate of calcium oxalate is the trihydrate (COT), followed by dihydrate (COD),monohydrate (COM), the most stable form of the three. Therefor, the most commonly found crystals in kidney stones is COM [9]. Although less stable, COD can also be found, yet in lower probability, whilst COT is rarely present as kidney stones.

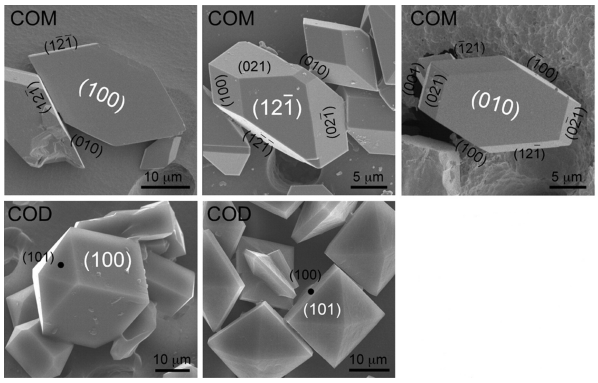

Figure 1.3: Different kinds of calcium oxalate hydrates[10]

1.2.3. TREATMENT

There are several way to treat urolithiasis, but not every case of kidney stone needs medical attention. The physician will always first check how big the stone has grown and where it is located before making a decission the kind of treatment to proceed on. Small stones that are up to a size of 5 mm can pass through the body naturally [11]. For stones bigger than 5 mm methods like Extracorporeal shock wave lithotripsy (ESWL) can be used. ESWL is a technique that removes kidney stones without having to invade the body of the patient. Using a lithotriptor machine, high intensity pulses are applied externally onto the body of the patient. This will result in fracturing of the stones into smaller sizes which can leave the body naturally [12].

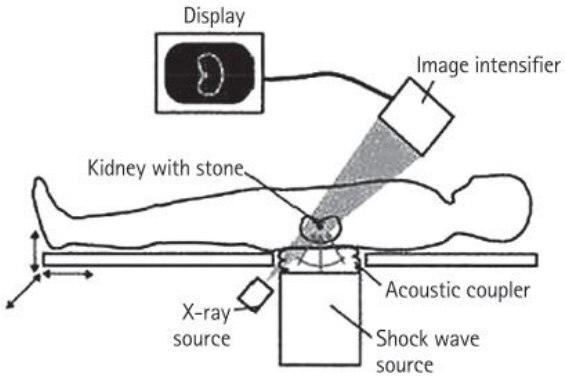

Figure 1.4: ESWL schematic[8]

Another technique to remove kidney stones is Ureteroscopy. This method uses a ureteroscope, which is a thin telescopic medical instrument. The ureteroscope will be inserted in the urethra, through the bladder and then into the ureter. The stone will be removed gently through the ureter and the urethra or broken up into small pieces by a laser [13].

The last method is called percutaneous nephrolithotomy (PCNL) where a small incision is made in the back of the patient. Through this small incision a nephroscope, A thin telescope, is inserted into the kidney. After discovering the exact location of the stone, it can be removed through the incision made for the nephroscope. There is also the option of breaking up the stone with a laser and let the small pieces pas through naturally [14].

1.3. THESIS OBJECTIVES

In this project the main goal is to find the induction time of calcium oxalate formation which is the primary constituent of kidney stones. Using the induction time data the nucleation rate can be calculated for calcium oxalate which is a important value to understand not only the formation of kidney stones but also the blocking of the kidney channels. When the time needed for supersaturated urine to pass through the body is longer than the nucleation time, then there is a chance that nucleation can happen inside the urinary tract and grow.

To reach this goal induction time experiments should be conducted. Induction time experiments can be done in several kinds of ways, but statistics has shown that there should be a minimum limit of 80 data points to get an accurate result of the induction time. In this project the induction time will be measured in lab size reactors and in microfluidic devices. The two obtained results will be compared with each other. For the lab scale experiment, a combination of the easymax and the Focused beam reflectance measurement (FBRM) will be used. The microfluidic experiments need to be set up from the beginning by designing a whole new microfluidic system.

2

LABORATORY-SCALE EXPERIMENTS

2.1. THEORETICAL BACKGROUND

2.1.1. SUPERSATURATION

For crystallization to occure, a driving force is needed in the form of supersaturation. To achieve this supersaturation different kinds of methods can be applied such as cooling and evaporation. A solution is saturated when both the chemical potential of the crystal phase μ_C and the chemical potential of the solute μ_S^* are equal to each other, as can be seen in equation 2.1 [15]. The saturated points are represented as a black line in the solubility diagram (figure 2.1).

$$\Delta\mu = \mu_S^* - \mu_C = kTln(S) \tag{2.1}$$

Supersaturation ratio equation 2.2 is usually used to calculate if the solution is supersaturated, where the C is defined as the dissolved compound concentration and the C^* is the solubility under normal equilibrium conditions. If the supersaturation ratio exceeds 1 then the solution is supersaturated, if the ratio is below 1 then it is undersaturated.

$$S = \frac{c}{c^*} \tag{2.2}$$

In figure 2.1 it becomes clear how a supersaturation is reached by cooling or evaporation. Once a solution crosses the solubility line towards the metastable region, by either evaporation of the solvent or decreasing the temperature, this solution is supersaturated and prone to nucleation. If the supersaturation keeps on increasing, it will eventually reach the labile zone and nucleate. Although, it is not mandatory for the solution to reach this point to nucleate.

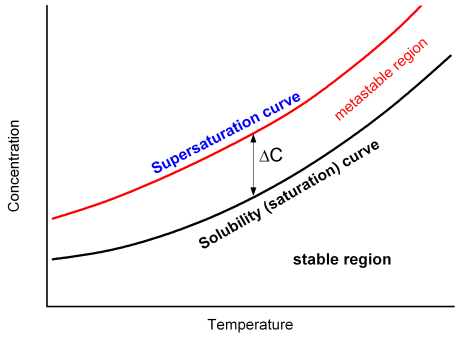

Figure 2.1: Solubility diagram

2.1.2. NUCLEATION

Nucleation is the first step in the formation of crystals with supersaturation as its driving force. Nucleation can be separated and categorized into two different mechanisms.

PRIMARY NUCLEATION

The first mechanism is called primary nucleation. This mechanism happens when there is a solution where initially no crystals are present. Primary nucleation can be divided into two subcategories, homogeneous and heterogeneous nucleation. According to the Classical primary nucleation theories, homogeneous nucleation referes to a mechanism where molecular collision and interactions result in a lattice-structured body with a chance of achieving thermodynamic stability [16].

Heterogeneous nucleation refers to a mechanism where foreign substances or particles initiate the nucleation. The mechanism on how the foreign particles initiates the nucleation is not well understood. One of the hypothesis is that the particle adsorps the solute on its surface where nuclei start to develop and continues to grow into a macrocrystal [16].

Homogeneous nucleation

According to the classical nucleation theory homogeneous nucleation happens when the total free energy change reaches its critical point and starts decreasing. Using equation 2.3 it is possible to calculate the total free energy change [17]. In this equation the first term of the right hand side represents the gibbs free energy contributed by the formation of solid-liquid boundaries [18], where γ is the surface free energy and r the radius of a cluster. The second right hand side term represents the volume contribution [16], where the n_i is the number density and $\Delta\mu$ is the difference in chemical potential (equation 2.1). Combining these two contributions gives the total free energy change. The two contributions and the total free energy are plotted in figure 2.2, where the red dotted line represents the surface contribution, the blue dotted line represents the volume contribution and the green line represents the total free energy.

$$\Delta G = 4\pi r^2\gamma - \frac{4}{3}\pi r^3 n_i \Delta\mu \tag{2.3}$$

For cluster to be stable and grow, its size needs to be larger than the critical radius. The critical radius can be calculated by equation 2.4, which was obtained by finding the derivative of equation 2.3 and set it equal to zero. When the size of a cluster is smaller than the critical radius, it is called an embryo. Embryos will not grow larger but gets dissolved back into the solution instead. Clusters that are larger than the critical radius will keep on growing and is called a nuclei.

$$r^* = \frac{2\gamma}{n_i \Delta\mu} \tag{2.4}$$

As can be seen in figure 2.2 a certain amount of activation energy ΔG^* must be provided for the cluster to be stable and continue growing. This activation energy can be calculated by combining equations 2.1, 2.3 and 2.4.

$$\Delta G^* = \frac{16\pi\gamma^3}{3n_i^2\Delta\mu^2} = \frac{16\pi\gamma^3}{3n_i^2 k^2 T^2 ln^2(S)} \tag{2.5}$$

By taking the Arrhenius form of Nucleation rate J and substituting the activation energy from equation 2.5 gives

$$J_{homogeneous} = Aexp\left(-\frac{\Delta G^*}{kT}\right) = Aexp\left(-\frac{16\pi\gamma^3}{3n_i^2 k^3 T^3 ln^2(S)}\right) = Aexp\left(-\frac{B}{ln^2(S)}\right) \tag{2.6}$$

In this equation the A represents the pre-exponential factor, which are the kinetic parameters and B represents the thermodynamic parameters [19].

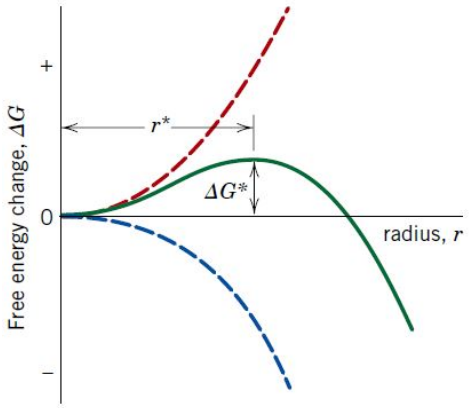

Figure 2.2: A schematic plot of gibbs free energy versus the radius of clusters[18]

In practice, homogeneous nucleation is hard to achieve. When a crystallization experiment is set up there will always be some foreign particles in the solution which are impossible to prevent from getting in. Even if the solution is clear from any foreign particles the mechanical stirrers or vessel walls can initiate the process leading to heterogeneous nucleation.

Heterogeneous nucleation
Heterogeneous nucleation happens when nuclei form on a existing surface in the solution. This is due to the fact that the activation energy is lowered by a reduction in the surface free energy. In figure 2.3 a comparison is made between the activation energy of homogeneous and heterogeneous nucleation. As can been seen the energy barrier that heterogeneous nucleation needs to overcome is far lower than that of homogeneous nucleation.

When the two nucleation rates are compared (equation 2.6, 2.7) it can be seen that there are two differences, one is the pre-exponential factor and the second one is the surface free energy. Instead of the surface free energy of a whole particle, only the effective surface energy is taken.

$$J_{heterogeneous} = A_{HEN} exp(\frac{W^*_{HEN}}{kT}) = A_{HEN} exp\left(-\frac{16\pi v^2 \gamma^3_{eff}}{3k^3T^3 ln^2(S)}\right) = A_{HEN} exp\left(-\frac{B_{HEN}}{ln^2(S)}\right) \tag{2.7}$$

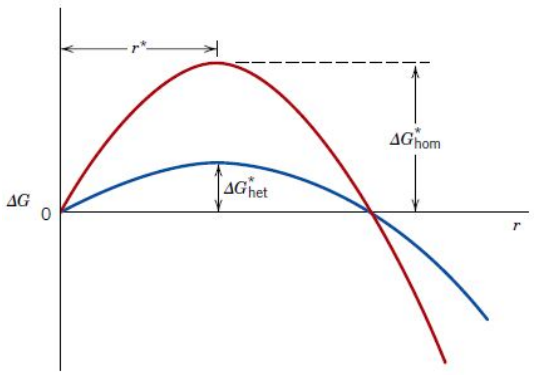

Figure 2.3: Schematic of the gibbs free energy over cluster radius for heterogeneous and homogeneous nucleation[18]

The effective surface energy can be calculated by rearranging Young's law (equation 2.8) into equation 2.9. In figure 2.4 a schematic is given of a heterogeneous nucleation with surface tensions indicated that are used in Young's law. Young's law exist of 3 different surface tensions, solid-liquid γ_{SL}, solid-interface γ_{SI}, interface-liquid γ_{IL} and the wetting angle θ.

$$cos\theta = \frac{\gamma_{IL} - \gamma_{SI}}{\gamma_{SL}} \tag{2.8}$$

$$\gamma_{eff} = \gamma_{SL} = \frac{\gamma_{IL} - \gamma_{SI}}{cos\theta} \tag{2.9}$$

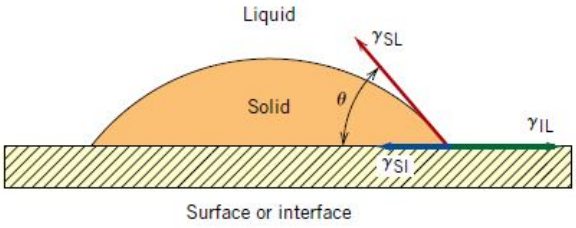

Figure 2.4: Schematic of heterogeneous nucleation[18]

SECONDARY NUCLEATION

Secondary nucleation only happens when there are crystals present in the solution from the same species. These crystals will induce the nucleation on its surface or undergo attrition. Attrition causes breakage of crystals by collision between crystals and the vessel wall, mechanical agitators or other crystals. For attrition to occure the crystal present needs to be larger than a certain size [16].

2.1.3. GROWTH

After a nuclei has exceeded the critical radius point it will continue onto the growth phase. There are two steps in crystal growth, mass transport and surface reaction. In the mass transport step molecules and atoms are transported from the bulk solution to the surface of the crystal. The second step is surface reaction where growth units are integrated into the crystal lattice [16].

2.1.4. AGGLOMERATION

Particles which are suspended inside a liquid can grow by agglomeration. This is when at least two particles get into contact with each other for a time long enough for them to be bound to one another. Kidney stones are not only composed of calcium oxalate but agglomerate of calcium oxalate, polysaccharides, lipids, protein and other cell-derived material [20].

2.1.5. INDUCTION TIME

Nucleation is a stochastic process, also called a random process, which means that each experiment with identical conditions yields different results. With independent experimental results the probability P_m of nucleation can be described by the Poisson distribution 2.10:

$$P_m = \frac{N^m}{m!} exp(-N) \tag{2.10}$$

In this equation N stands for the average number of nuclei formed inside a supersaturated solution and m is the number of nuclei formed in a time interval. Using equation 2.10 and filling in $m = 0$ an equation can be obtained for a probability P_0 where no nuclei are formed.

$$P_0 = exp(-N) \tag{2.11}$$

With P_0 the probability $P_{\geq 1}$ of an experiment nucleating at a specific time can be calculated with the following formula:

$$P_{\geq 1} = 1 - P_0 = 1 - exp(-N) \tag{2.12}$$

There is a relation between the average number of nuclei formed and the stationary nucleation rate J at a specific time interval t_J and volume V. This relation is given in equation 2.13.

$$N = JVt_J \tag{2.13}$$

Combining equation 2.12 and 2.13 gives a new equation for the probability $P_{\geq 1}$ where at least one nuclei is formed in the time interval t_J.

$$P^*_{\geq 1} = 1 - exp(-JV t_J) \tag{2.14}$$

A nuclei has to grow to a certain size before it can be detected, this is the limitations of the machines used for analyzing the nucleation. To incorporate this delay the following equation can be used for t_J:

$$t_J = t - t_g \tag{2.15}$$

In this equation t is the time of detection and t_g is the delay time or the growth time until the nuclei is detectable. The corrected probability $P(t)$ can be determined by equation 2.16.

$$P(t) = 1 - exp(-JV(t - t_g)) \tag{2.16}$$

This equation can be further simplified by introducing the mean induction time τ. This equation 2.17 is derived from equation 2.13 and 2.15, where the assumptions are made that a single nuclei is formed and the delay time t_g is negligible.

$$\tau = \frac{1}{JV} \tag{2.17}$$

By substituting equation 2.17 into equation 2.16, the final probability $P(t)$ equation 2.18 is derived. This is an exponential model and used for nucleation at constant rates.

$$P(t) = 1 - exp\left(-\frac{t - t_g}{\tau}\right) \tag{2.18}$$

To determine the probability $P(t)$ from experimental values, a large number of induction time experiments should be performed under the same conditions. With the obtained experimental values, the following equation can be used to calculate the probability [21]:

$$P(t) = \frac{M^+(t)}{M} \tag{2.19}$$

Where $M^+(t)$ is the number of experiments where nucleation has taken place/detected at time t and M is the total amount of experiments performed.

2.1.6. WEIBULL

Weibull is another model which is used for different kinds of nucleations such as one with a decreasing rate, but can also be applied to a nucleation with a constant rate. The Weibull model is described by equation 2.20 as shown below:

$$P(t) = 1 - exp\left(-\frac{t}{\tau}\right)^k \tag{2.20}$$

In this equation t is the detection time, τ is a time scale related to the median nucleation time and k is the shape parameter. The shape parameter says something about the nucleation rate, when $k = 1$ the Weibull model reduces to an ordinary exponential model. For $k < 1$ the nucleation rate is decreasing and for $k > 1$ the nucleation rate is increasing [22]. The median nucleation time can be calculated using equation 2.21.

$$\tau = t_{med}(ln2)^{1/k} \tag{2.21}$$

2.1.7. FOCUSED BEAM REFLECTANCE MEASUREMENT

For lab-scale experiments an analytical device called the FBRM is used. The FBRM is an inline measurement device that measures the counts and chord size. The way this device works is by shooting a focused laser beam right outside the probe's sapphire window. When there is a particle, the laser beam will be reflected back into the probe where there is a detector. The longer the laser gets reflected the bigger the chord size is [23].

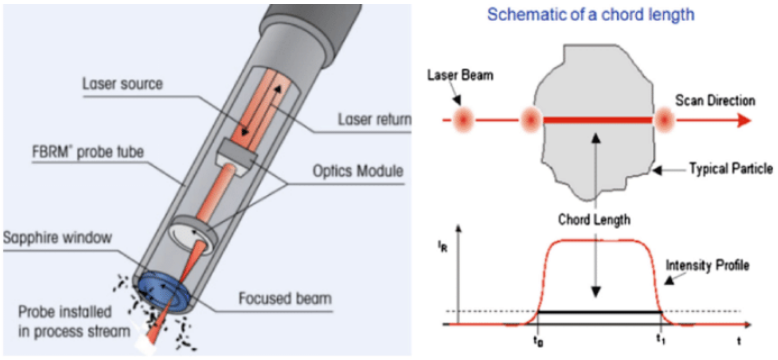

Figure 2.5: Schematic of the FBRM probe [24]

2.2. MATERIALS AND METHODS

2.2.1. MATERIALS & EQUIPMENT

Table 2.1: Chemicals used in lab scale experiments

	Chemical Formula	CAS Number	Vendor
Potassium Oxalate Monohydrate	$(COOK)_2 \cdot H_2O$	6487-48-5	Sigma-Aldrich
Calcium Chloride	$CaCl_2$	10043-52-4	Sigma-Aldrich
Ultra pure Water	H_2O	-	Elga

Table 2.2: Equipment used in lab scale experiments

Equipment	Equipment Name	Brand
Scale	-	Mettler Toledo
Particle tracker	Focused Beam Reflectance Measurement	Mettler Toledo
Reactor	EasyMax 102 Advanced Synthesis Workstation	Mettler Toledo
Heating plate	-	iDL

2.2.2. SOLUTION PREPARATION

Before making the solutions, the amount of chemicals needed is calculated by backcalculations using the supersaturation equation 2.22. In this equation K_s is the solubility of calcium oxalate monohydrate, which was taken to be 2.74 mol/L according to W. McComas et al. [25].

$$Supersaturation\ ratio = \sqrt{\frac{[Ca^{2+}][Ox^{2-}]}{K_s}} \tag{2.22}$$

By picking a specific supersaturation ratio, it is possible to calculate the necessary amount of calcium chloride and potassium oxalate. A scale was used to weigh the chemicals and water needed to make the calculated supersaturation. To be sure that the chemicals are dissolved an ultrasonicater is used to break off all the compounds into ions. A small amount of solution is made each time and will not be reused after leaving it overnight to eliminate the risk of contamination.

2.2.3. EXPERIMENTAL CONDITIONS

The measurement were performed using FBRM in combination with the easymax reactor. For this experiment a mixture was made with 35ml of both calcium chloride and potassium oxalate solution and 30ml of water [26]. The temperature of the reactor was set to 37 degrees Celsius and the stirrer was set to 300rpm. The running time of the experiments depends on the supersaturation used. To get a accurate measurement one of the solution is mixed with water and added to the reactor first. After adding the solution and water

Table 2.3: Amount of chemical needed to prepare the supersaturated solutions for lab scale experiments

Supersaturation ratio	Calcium chloride (mg/100ml solution)	Calcium chloride (mmol/L)	Potassium oxalate (g/100ml solution)	Potassium oxalate (mmol/L)
33	9.89	0.89	14.81	0.89
35	10.55	0.95	15.79	0.95
37	11.01	0.99	16.79	1.01

the FBRM and the easymax were started, at this point the second solution was added to the reactor. This sequence is necessary to eliminate the possibility of nucleation while starting up the machines.

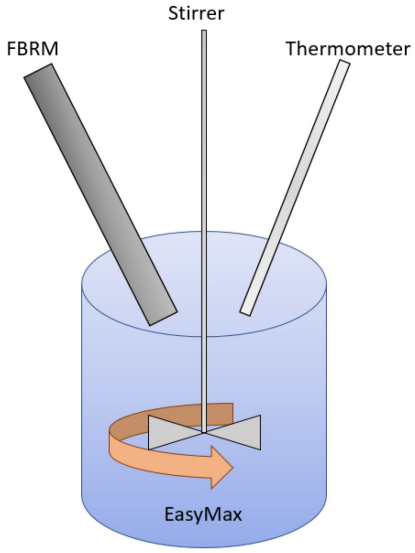

Figure 2.6: Schematic FBRM setup[27]

2.3. RESULTS & DISCUSSION

For the lab scale experiments supersaturation ratios 33, 35 and 37 were used. These three supersaturation ratios were carefully chosen after a set of experiments, were a wide range of ratios were tested. After doing these tests a decision has been made according to the time needed for the solution to nucleate. For plotting and fitting the data a matlab code was used, which can be found in appendix A.

In figure 2.7 The experimental data was plotted with the exponential model. This model is one of the relative easier models to use, but is limited to only fixed nucleation rates. As can be seen in the figure, the exponential model does not fit all the supersaturation ratios. The model fits for both the supersaturation ratios of 33 and 37, but gives a bad fit for supersaturation ratio 37. This can be cause due to the lack of data point obtained from the FBRM lab scale experiments. Another reason could be that the experimental condition were not the same for every data point, this will lead to wrong results. Every data point uses freshly made solution and these solutions. Even though made carefully, the concentration can be different each time.

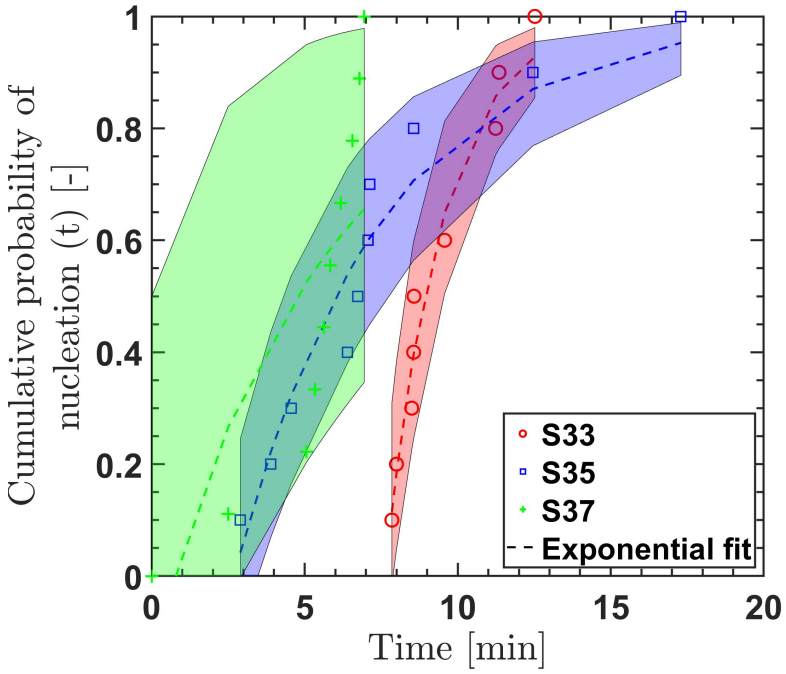

Figure 2.7: Probability curves at different supersaturation ratio fitted with the exponential model

In table 2.4 the obtained parameters of the exponential model is given after fitting the model into the experimental results. An increase in supersaturation ratio should resulting in a decrease in induction time τ is expected. But this is not the case with the exponential model fitted into the experimental data from the FBRM. The induction time increases with a increase in supersaturation ratio. This can not be true, because supersaturation is the driving force for crystallization. That means that the driving force is bigger at a higher supersaturation ratio, leading to a shorter induction time.

Table 2.4: Parameters t_g and τ from exponential model fitted into the probability distribution at different supersaturation

Supersaturation ratio	t_g	**95% confidence interval**	τ **(min)**	**95% confidence interval**
33	7.62	7.36, 7.88	1.86	1.32, 2.40
35	2.70	1.94, 3.45	4.78	3.41, 6.15
37	0.69	-1.52, 2.89	5.87	2.20, 9.54

This is the reason why the Weibull model has been used for curve fitting. This model is more difficult compared to the exponential model, but is applicable for different kinds of nucleation rates. In figure 2.8 the

experimental results have been plotted again, but this time with the Weibull model fitted through the data points. This shows a curve that fits the experimental results better for all the supersaturation ratios.

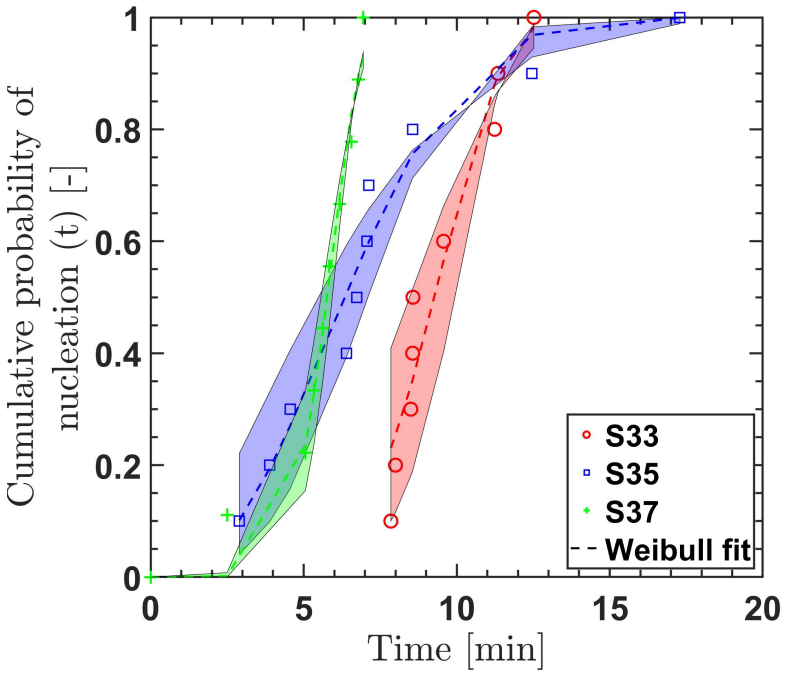

Figure 2.8: Probability curves at different supersaturation ratios fitted with the Weibull model

In table 2.5 the Weibull parameters obtained after fitting the model were tabulated. The induction time shows a decreasing trend with an increase in supersaturation ratio, which is what to be expected. When looking at the parameter k for all of the supersaturation ratios, it can be seen that all of them are above one. This means that the nucleation rate for this process is a increasing nucleation rate.

Table 2.5: Parameters k and τ from exponential model fitted into the probability distribution at different supersaturation

Supersaturation ratio	k	**95% confidence interval**	τ **(min)**	**95% confidence interval**
33	5.82	3.66, 7.99	9.88	9.35, 10.40
35	2.38	1.62, 3.15	7.40	6.83, 7.98
37	7.21	5.59, 8.83	6.07	5.94, 6.19

With the Parameters k and τ known, the median time can be calculated with equation 2.21. This median nucleation time is used in equation 2.17 to calculate the nucleation rate. In table 2.6 below, the median nucleation time and the nucleation rates are tabulated. The nucleation time shows a increasing trend when the supersaturation ratio increase, which is to be expected.

Table 2.6: The calculated median nucleation time and nucleation rate for the 3 different supersaturation ratios

Supersaturation ratio	**Median nucleation time (min)**	**J** $(nuclei\ s^{-1}\ L^{-1})$
33	10.52	0.016
35	8.63	0.019
37	6.38	0.026

After obtaining the nucleation rate J, the kinetic and thermodynamic parameters can be determined by plotting $log(J/S)$ versus $log^2(S)$. This was derived from equation 2.6 or 2.7 and will give a linear curve if this process follows the classical nucleation theory. When a linear curve is fitted through the 3 data points, the

slope represent the kinetic parameter and the y intercept will represent the thermodynamic parameter. In this case, the kinetic parameter will be -14.1 and the Thermodynamic parameter will be 4.87.

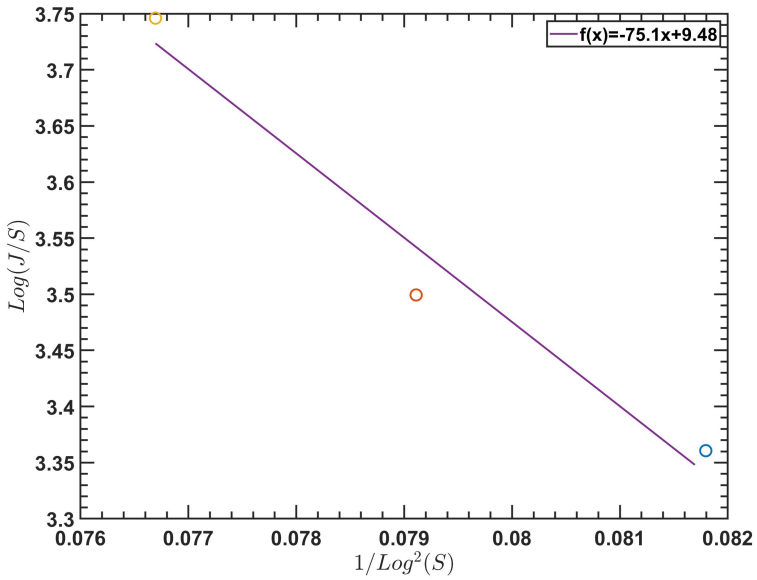

Figure 2.9: Logarithmic plot of J/S versus S to obtain the kinetic and thermodynamic parameters

3

Design and Production of Microfluidic Devices

As mentioned before nucleation is a stochastic process, which means that multiple data points are needed to determine the induction time. This is a time consuming process if done with lab scale experiments. This is the reason for introduction of a new method to perform these measurements. With droplet sized micro reactors in micro channel, more than hundreds of experiments can be performed at the same time. This will reduce the time needed to perform the experiments and increase the data point obtained.

For the microfluidic experiments a new chip have been designed with solidworks. A couple of requirements has to be met while designing the mould:

- The chip needs three inlets, two for the solutions, one for the continuous phase and one outlet.
- There should be a T, Y or K shaped junction to create droplets.
- The chip needs bends in the beginning to mix the two solutions inside the droplets.
- The chip should have a capacity of at least 100 droplets.
- The design should fit inside the printing platform of the 3D printer(43x27 mm).

3.1. Theoretical background

3.1.1. 3D printer

The printer used for printing the moulds is a digital light processing (DLP) printer. This kind of 3D printer was chosen for its high accuracy. The printer uses prefactory RP to slice the 3D design into thin slices, which will be printed by the printer.

The three main components of a DLP printer are illustrated in figure 3.1. There is a platform where the object will get printed on. This platform will move out of the liquid resin each time one layer has been printed, this happens to refresh the liquid under the print. The second component is the projector which projects the image onto the platform using an industrial UV light. The last component is the reservoir which holds the liquid resin that is used as printing material. The liquid resin is a mixture of a monomer, initiator and a catalyst. This mixture will form covalent bond while exposed to UV light [28].

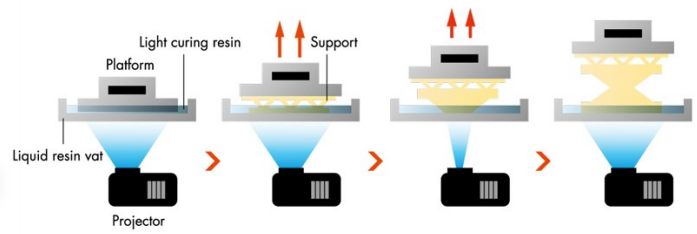

Figure 3.1: Schematic of a DLP printer [29]

The DLP printer used in this project is from a company called envisiontec, model Micro Plus Hi-Res as shown in fig 3.2. This model has a x and y axis resolution of 30 microns and a z axis resolution of 25 microns. The maximum printing size is 43 by 27 millimeters [30]. The Micro Plus Hi-Res uses HTM140 as printing liquid. This is a high temperature mold material with a heat deflection temperature of 140 degrees Celsius. HTM140 is applicable in many fields such as aerospace, automotive and manufacturing. After printing an object, it needs additional curing in a separate curing unit (figure 3.3). The curing unit outputs a UV light of 320 to 550 nanometers, which is able to cure the 3d printed object.

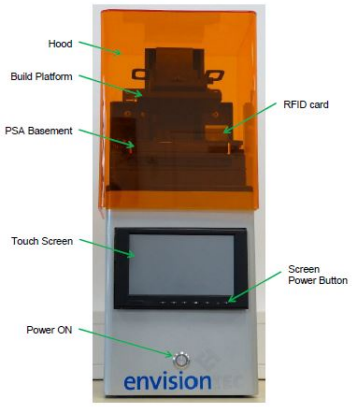

Figure 3.2: Envisiontec optical resin curing 3D printer [30]

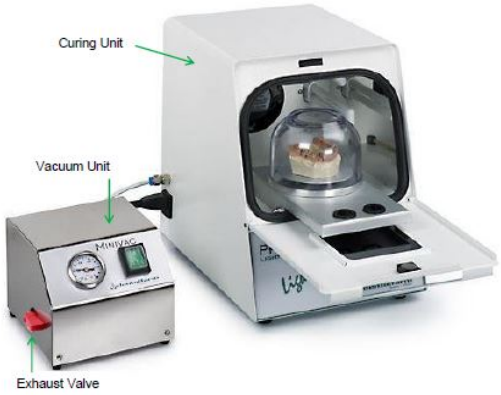

Figure 3.3: Curing machine for 3D printed objects [31]

3.1.2. DROPLET FORMATION

To make these small droplet sized micro reactor, which will behave like a batch reactor, a K-junction is used. K-junction is a modified version of the well known T-junction. These kind of junction creates a slug flow out of two immiscible fluids. These droplets sized reactors are great for induction time experiments, since the small size gives a better mass and heat transfer. Using this method also gives equal sized droplets which makes all the experiments have the same conditions.

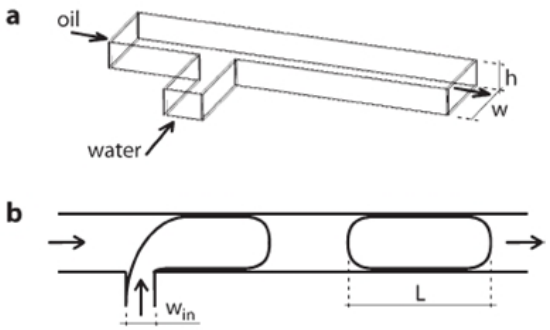

Figure 3.4: Droplet formation inside a micro channel with a T junction, a. shows the junction in 3d b. shows how the droplets are formed[32]

As shown in figure 3.4 there is a oil continuous phase and aqueous disperse phase. When the continuous phase is flowing it will block off the dispersed phase, this will lead to a pressure build up in the dispersed phase channel. At some point the pressure that has been building up of the dispersed phase will be bigger than the continuous phase and start flowing, which will block off the continuous phase. After a while the pressure in the continuous phase will be bigger again and so the sequence will repeat.

3.1.3. DROPLET MIXING

There are different methods for mixing inside microfluidic devices. The method choosen for this design is chaotic advection due to microchannel geometry, based on the work by Ottino [33]. By implementing bends into the microfluidic design the drag force will create different flows inside the droplets, where in case of a straight channel the mass transfer will only occur laminar flow as shown in figure3.5.

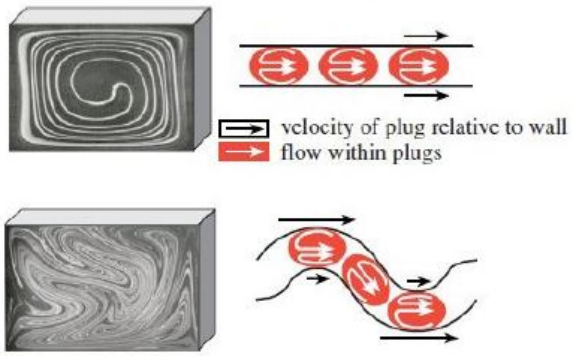

Figure 3.5: Mixing flow of droplets in microfluidic bends[33]

To quantify the mixing inside microfluidic droplets, the Danckwerts number can be calculated as shown in equation3.1[34]. In this equation the Danckwerts number θ is calculated using the total number of pixels M, the intensity of a pixel I_n and the average intensity $\overline{I}$.

$$\theta = \frac{\sqrt{\frac{1}{M}\Sigma_{n=1}^{M}(I_n - \overline{I})^2}}{\overline{I}} \tag{3.1}$$

A high Danckwerts number means insufficient mixing. As the droplet continues to get mixed the Danckwerts number will decrease and eventually reach a constant value. In figure 3.6 it can be seen how well a droplet is mixed after a certain amount of bends at different flow rates. After 5 bends a droplet can be assumed as homogeneously mixed.

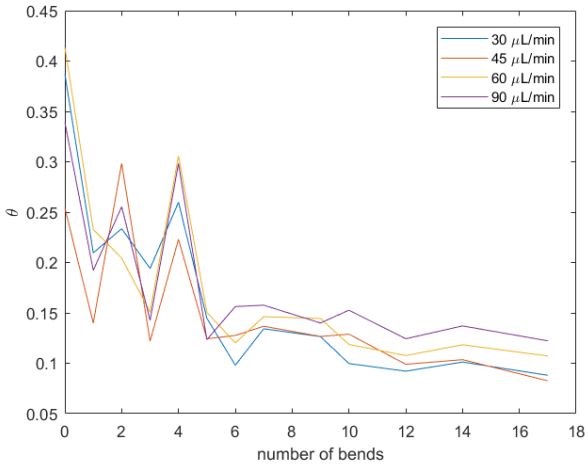

Figure 3.6: Intensity of segregation versus number of bends[35]

3.2. MATERIALS AND METHODS

3.2.1. MATERIALS & EQUIPMENT

Table 3.1: Chemicals used in microfluidic device process

	Chemical Formula	CAS Number	Vendor
Ultra pure Water	H_2O	-	Elga
HTM140	-	-	Brilliant Technology B.V.
Trichlorosilane	$CF_3(CF_2)_5CH_2CH_2SiCl_3$	78560-45-9	Sigma-Aldrich
PDMS	$(CH_3)_3Si[OSi(CH_3)_2]_nOSi(CH_3)_3$	-	The DOW Chemical Company
2-propanol	C_3H_8O	67-63-0	Sigma-Aldrich
NOA61	-	-	Norland
Indigo Carmine	$C_16H_8N_2Na_2O_8S_2$	860-22-0	Sigma-Aldrich

Table 3.2: Equipment used in microfluidic device process

Equipment	Equipment Name	Brand
Sonicator	2510 Ultrasonic Cleaner	Branson
Oven	-	Binder
Heating plate	-	iDL
Optical resin curing printer	EnvisionTEC Micro Plus Hi-Res	EnvisionTEC
Spincoater	Polos 300 spin coater	Spincoating

3.2.2. 3D PRINTING

The design for the mould that has been made in solidworks need to be printed next. Printing will be done in the EnvisionTEC Micro Plus Hi-Res. This printer uses a high temperature mould material to print which has a resolution of 30 microns in the x and y direction and a resolution of 25 microns in the z direction. After printing, the mould should be cleaned thoroughly with isopropanol and ultrasonicator if needed. After cleaning off all the HTM residue, the mould can be cured in the light curing furnace. This machine send outs UV light which fully cures the mould. The mould should be cured in the furnace for at least 4 minutes, after fully curing the mould can be used directly.

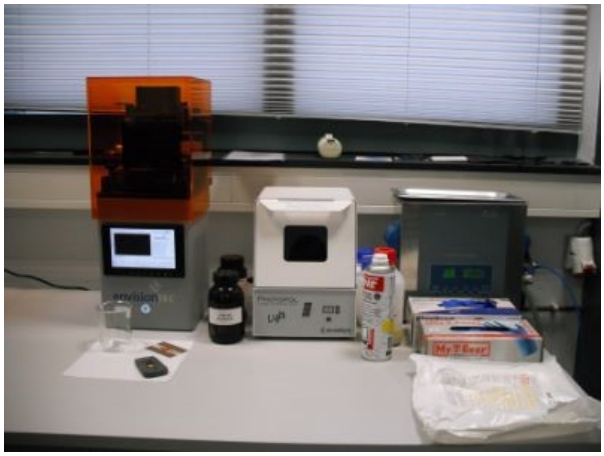

Figure 3.7: 3D printer setup

3.2.3. HYDROPHOBIZATION

The 3D printed mould is hydrophobized before use to make the process of pealing the PDMS off the mould more easy. For this process the chip should be cleaned with methanol and dried afterwards. After cleaning the mould it will be placed inside a desiccator with three drops of Trichlorosilane in a glass petridish. The

pressure inside of the desiccator will be reduced to 100 mbar by connecting it to a pump and set aside for 2-4 hours. After hydrophobization the mould can be used for at least 4-5 times before this process should be repeated.

3.2.4. PDMS CHIP FABRICATION

For PDMS chip fabrication, the intial step consists of mixing 1 part curing agent to 7 parts of elastomer, the mixture has to be mixed until it turns turbid. After mixing, the mixture will be centrifuged at 7400rpm for 15 min to get rid of the air bubbles and possible dust particles. The PDMS has to be used right away or stored in the fridge if not and can be used upto 4 hours after preparing. To produce the PDMS chip, the hydrophobized mould is placed inside a glass petridish. The petridish will be filled with the PDMS, which was made beforehand, until the mould is fully submerged. After pouring the PDMS there will be air bubbles between and on the mould, these air bubbles needs to be removed before curing. To remove these air bubble the petridish is put into a desiccator. The pressure will be reduced to 100 mbar by connecting it to a pump and set aside for 30 min. When all the air bubbles has been removed, the chip can be cured. The curing process will be done inside a oven at 65 $^{\circ}C$ for 12 hours. This process can also be sped up by increasing the temperature to 90 $^{\circ}C$ and keeping it in the oven for 20 min. After 12 hours or 20 min of curing the chip can be peeled off the mould. After peeling the inlet and outlet holes are made with a blunt tip syringe.

3.2.5. SPINCOATING AND SEMI-CURING

To stick the PDMS chip on a microscope slide to complete the channel, it is necessary to spincoat a thin layer of PDMS onto the glass slide first. This layer of PDMS will act as a glue layer that sticks the PDMS chip to the glass slide. To spincoat, first a PDMS mixture should be made just like for the chips but this time the ratio curing agent to elastomer should be 1:10 respectively. The reason for the difference is the control over the curing process, less curing agent means that the curing process will be slower. After making the PDMS mixture it can be used to spincoat. First 0.5 ml of PDMS mixture is put on a clean slide, which is put in a desiccator to remove air pockets. After doing so the slide can be put into the spincoater to run a program that is pre-installed.

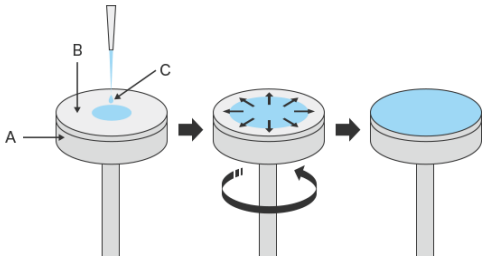

Figure 3.8: Process of spincoating

After spincoating the slides the hardest part comes, which is semi curing. This process has no fixed duration and needs to be checked on regular basis. If the slides are cured too far then the chip will not stick, but if it is not cured enough then the PDMS will seep into the channels and in worst case block the whole channel. The best way to check if the slide is semi cured is by touching the slide at the edge with a finger. The slide should feel sticky but not wet, if this is the case then the PDMS chip can be slowly put onto the slide. After putting on the slide a piece of tissue is put on top of the PDMS chip and then another glass slide on top, shown in figure 3.9. This is to prevent the PDMS chip from delaminating. The device will continue to cure inside the oven at 65 degrees Celsius for 12 hours or 20 min at 90 degrees Celsius.

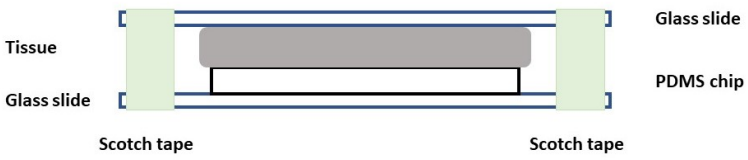

Figure 3.9: Schematic of sticking process

3.3. RESULTS & DISCUSSION

3.3.1. PRINTING PROCESS

As mentioned before, the platform of the 3D printer is raised out of the resin and dipped into the resin again after each layer printed. Initially the moulds would be printer at a zero degree angle, which means that the mould is parallel to the platform. When printed in this orientation there was a 90% chance that the mould would show defects. These defects will show up in the PDMS chips when used, as shown in figure 3.10.

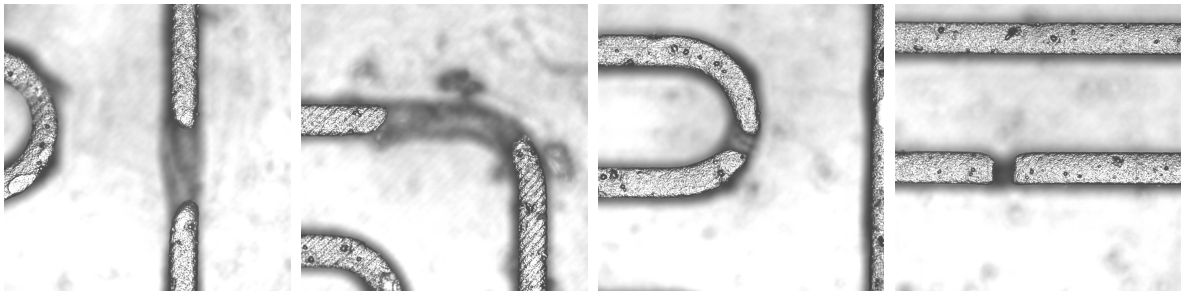

(a) Defect in outlet channel (b) Defect in outlet bend (c) Defect in channel bend (d) Defect in channel

Figure 3.10: Defects in several places of the microfluidic device caused by the defects in the mould

The cause behind these defects has later been identified as air bubbles being trapped underneath the print. This happens when the platform is raised out of the resin to refresh the resin under the print. To solve this problem, degassing holes were introduced into the design of the moulds. But after curing PDMS with these moulds, a new problem has emerged. When the liquid PDMS is poured inside the mould it will seep into the degassing holes. When cured it will create strings which will cause problems for later stages of making the devices.

The next solution was to print the moulds in an angle. When doing so the layers that gets printed each time is small enough to not trap air underneath. The first couple of moulds printed in an inclined angle did not have the defects anymore, but after making the microfluidic devices a problem emerged. There were capillaries created between the channels by printing it in an angle which resulted in a staircase like structure on the surface of the moulds. After optimizing the angle to 35 - 40 degrees, the mould would come out of the printer without defects and the finished devices will have not have capillaries between the channels.

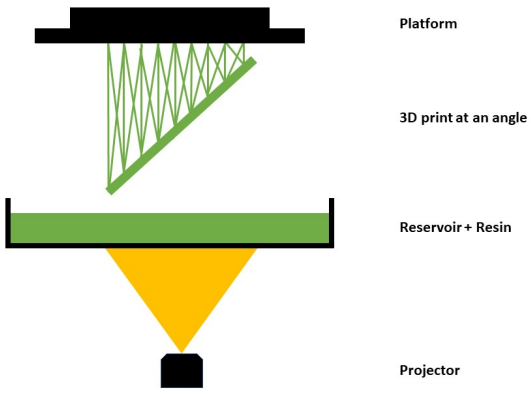

Figure 3.11: Schematic of printing at an angle

3.3.2. DIFFERENT DESIGNS

Over the course of the project, multiple designs have been made and tried out. In the following section the most important prototypes are given with a description and the reason behind the changes that were implemented. Figure 3.12 shows the initial design made by previous member of the research group P. van Tooren [36]. This design has one inlet for the continuous phase, one inlet for the dispersed phase and one outlet. The dimensions of the channels are 200 μm high, 200 μm wide and 1010 mm long. This design did not meet all the requirement, which were stated at the beginning of this chapter, needed to perform induction time experiments.

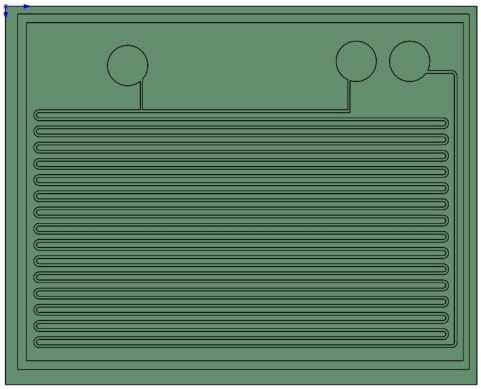

Figure 3.12: First design Made by P. van Tooren

The second design shown in figure 3.13 has one inlet more for the dispersed phase, so that both the calcium chloride and sodium oxalate can be pumped into the device at the same time. For the two solutions inside the droplet to mix, bendings were introduced right after the junction where the droplets are formed. The dimensions of this design is 200 μm high, 200 μm wide and 1024 mm long.

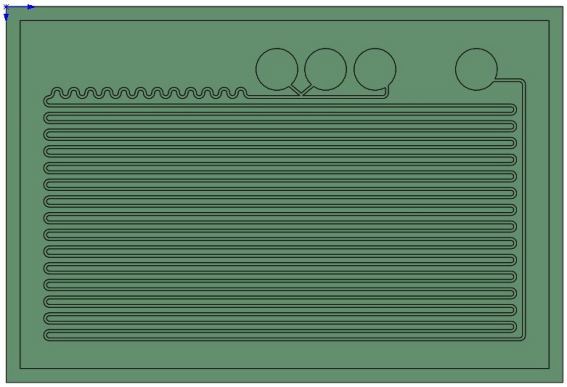

Figure 3.13: Second design with 3 inlets and mixing at the beginning

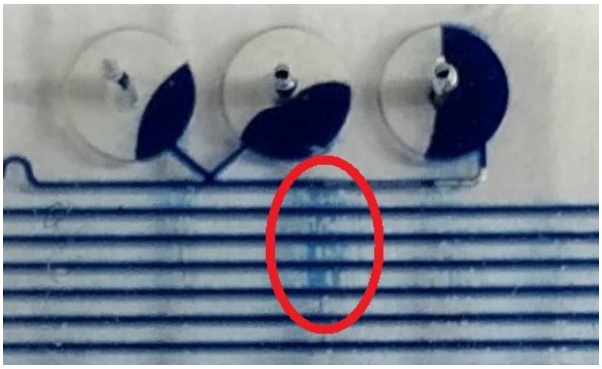

Figure 3.14: Bursting of the wall between channels

As can be seen in figure 3.14, blue liquid is seeping through the walls to the adjacent channel. The cause for the walls between two channels to burst is the applied pressure. This pressure is needed to make liquid flow inside the channels. But the resistance is too high which made the pressure needed to flow the liquid high enough to burst the walls. In the third design this problem has been solved by increasing the width of the channels to 400μm. This change can not be done without sacrificing part of the length of the channel, which results in the dimensions 200 μm high, 400 μm wide and 459 mm long. The third design is illustrated in figure 3.15.

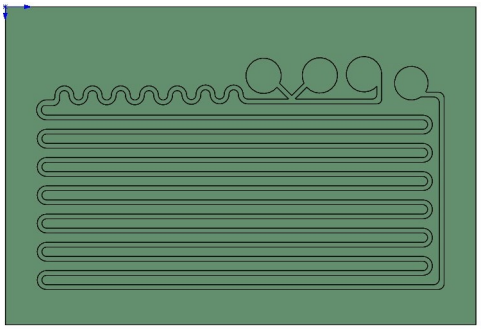

Figure 3.15: Third design with bigger dimensions of the channels

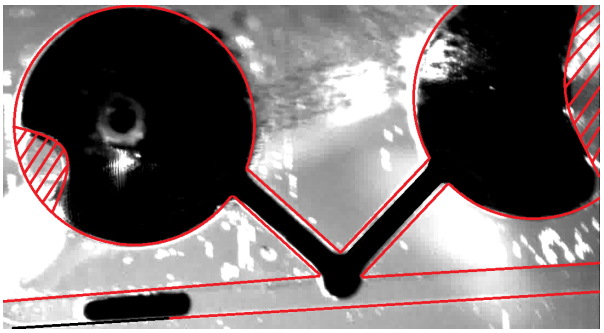

Figure 3.16: Air trapped in the inlet reservoirs

In figure 3.16 it can be seen that there is air trapped inside the inlet reservoirs. When compressable gasses gets trapped inside the reservoirs, the droplet formation will not be consistent. This means that droplet will either have different compositions and/or different sizes. To solve this problem, a smaller inlet is made into the design as shown in fig 3.17. The rest of the dimensions are kept the same as design three.

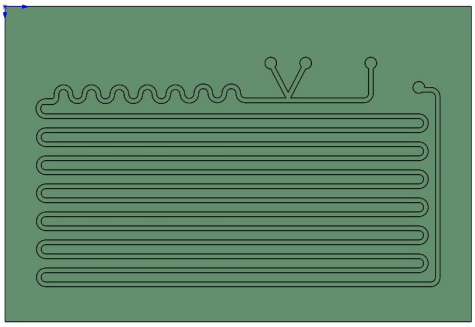

Figure 3.17: Fourth design with smaller inlets

For easy analysis the droplet should stay stagnant when the droplet formation is done and the flow is stopped. This is not the case with design four. When the pumps are stopped there should be no driving force to move the droplets, but a movement of the droplets in the channels is observed.

3.3.3. FINAL DESIGN

The driving force for the movement could not be found that is why a mould with chamber is designed, illustrated in figure 3.18. These chambers introduce a resistance high enough to stop the droplets from moving, as shown in figure 3.19. The dimensions of this design is 200 μm high, 400 μm wide and 427 mm long.

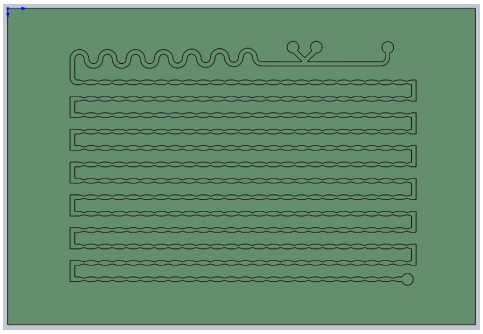

Figure 3.18: Final design of the microfluidic mould

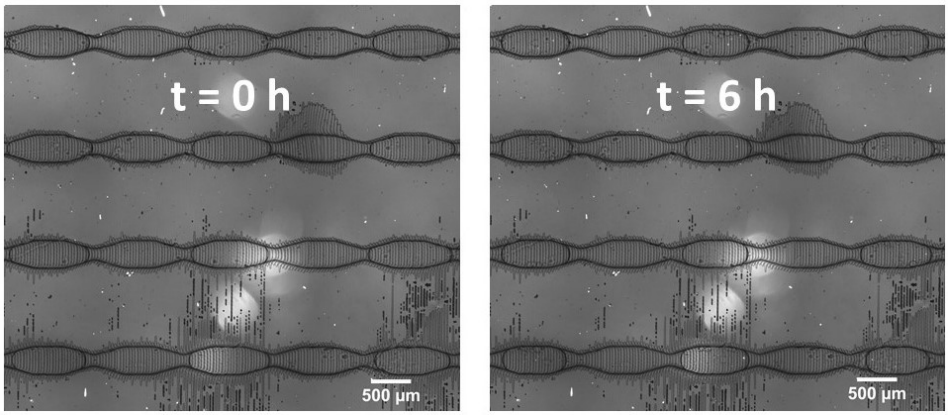

Figure 3.19: Droplet position at 0 hours and after 6 hours

In figure 3.20 the main part of the microfluidic device is illustrated. The microfluidic device can be divided into three zones, the droplet formation zone, the mixing zone and the storage zone. In the droplet formation zone, there are three inlets. One inlet for the continuous phase, one for the dispersed phase containing calcium chloride and one dispersed phase containing sodium oxalate. The K-junction where the droplets are formed is also in this zone. The next zone is the mixing zone where there is thirteen bends, these bends are responsible for inducing internal mixing in the droplets. The last zone is the storage. Here the droplets are trapped inside the chambers where they will stay stagnant for the rest of the experiment.

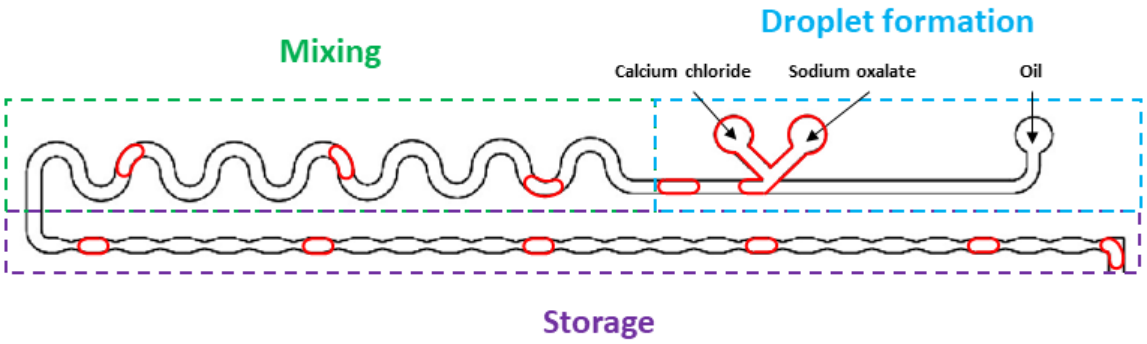

Figure 3.20: Description of the final design of the microfluidic mould

4

MICROFLUIDIC EXPERIMENTS

4.1. THEORETICAL BACKGROUND

4.1.1. DIMENSIONLESS NUMBERS

When looking at droplet formation and flow inside a microfluidic system, there are a couple of dimensionless numbers that are important to look into. These dimensionless numbers will be explained below.

REYNOLDS NUMBER

Reynolds number Re is a number that compares the inertial forces with the viscous forces, given as:

$$Re = \frac{\rho u L}{\mu} = \frac{inertial\ forces}{viscous\ forces} \tag{4.1}$$

In this equation ρ stands for the density given in $[kg/m^3]$, u is the velocity of the fluid flowing inside the channels given in $[m/s]$, L is the diameter of the microfluidic channel and μ is the fluid dynamic viscosity in $[Pa.s]$. When working with microfluidic channels the fluid velocities and length scales are usually small. This will give a low Reynolds number,$Re < 1$, which means that there is a laminar flow where the viscous forces are dominating the inertial forces.

CAPILLARY NUMBER

Another important dimensionless number, which gives information about the droplet formation is the capillary number. The capillary number Ca gives the relation between viscous forces and interfacial forces. The capillary number is given as:

$$Ca = \frac{\mu V}{\gamma} = \frac{viscous\ forces}{interfacial\ forces} \tag{4.2}$$

where γ stands for the surface tension between the continuous and the dispersed phase given in $[N/m]$. When the capillary number is high, $Ca > 10^-2$, the viscous force are dominating the interfacial forces. This will lead to a string of dispersed phase inside the continuous phase, where the breaking of droplet will not happen at the junction [37]. This phenomena is also called jetting. For low capillary numbers the interfacial forces are dominating the viscous forces. In this case the breaking of droplets will happen at the junction and is called squeezing or dripping depending on the geometry of the channels [32][38].

BOND NUMBER

The next important dimensionless number is the Bond number. This number gives the relation between gravitational forces and interfacial forces. The Bond number is represented as:

$$Bo = \frac{\Delta\rho g L^2}{\gamma} = \frac{gravitational\ forces}{interfacial\ forces} \tag{4.3}$$

Where $\Delta\rho$ is the density difference between the continuous and dispersed phase in $[kg/m^3]$ and g is the gravitational acceleration in $[m/s^2]$. Generally the Bond number in microfluidics is small, which implies that the interfacial forces are dominant [39]. This low gravitational force is caused by the small length scale in the numerator.

WEBER NUMBER

The last relevant dimensionless number is the Weber number. This number compares the inertial forces with the interfacial forces and is given as:

$$We = \frac{\rho v^2 l}{\gamma} = \frac{inertial\ forces}{interfacial\ forces} \tag{4.4}$$

If the Weber number is big the interface between the two liquids will deform and eventually break by the inertial forces. When the Reynolds number and the Weber number is small, the inertial forces can be neglected. This means that the capillary number will determine the droplet generation inside the microfluidic channels [40].

4.1.2. PRESSURE PUMP

Initially a syringe pump was used to perform the experiments. This pump uses a pushing block that pushes against a syringe which makes the liquid flow into the system. This method has some inaccuracies due to the mechanical limitations of the machine as shown in figure 4.1. This was the main reason to switch to the pressure pump.

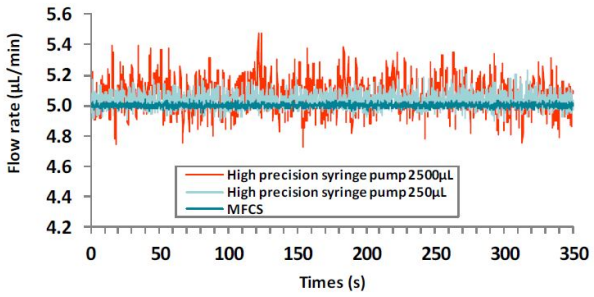

Figure 4.1: Fluctuations in flow rate of pressure pump compared to syringe pump [41]

Pressure pumps use gasses to build up pressure inside a reservoir filled with a solution. Increment in pressure will drive the liquid through a tubing to the device, as illustrated in figure 4.2 and 4.3.

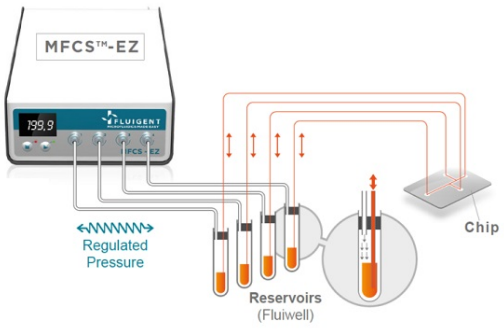

Figure 4.2: Schematic of the pressure pump setup [41]

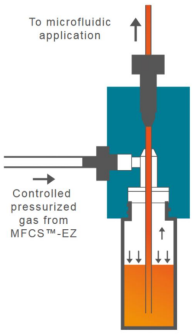

Figure 4.3: Schematic of the reservoir used by the pressure pump [41]

4.1.3. POLARIZED LIGHT MICROSCOPY

To get a better contrast between the crystals and the surroundings, polarized light microscopy was used. Normal light has vibrations in different directions. What the polarizer does is, it only lets light trough that vibrates in one specific direction. When the analyzer is aligned in the same angle as the polarizer the light can pass through. But when they are misaligned, the light will be blocked by the analyzer. If there is a specimen between the polarizer and the analyzer, the vibration will be redirected into another direction. This direction can be aligned with the analyzer so that the light will pass through. This means that only the specimen will light up while the surrounding stay dark.

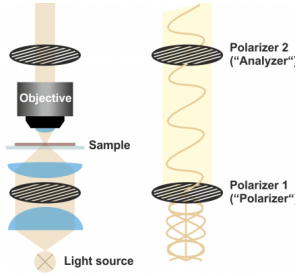

Figure 4.4: Parallel polarizers (polarizer and analyzer are aligned)

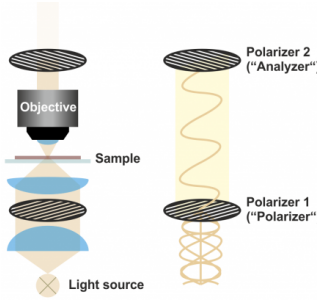

Figure 4.5: Crossed polarizers (polarizer and analyzer are misaligned)

This method of microscopy has been used to create a dark background with crystals that light up. To use polarized light microscopy two polarizing filters are used, one is called the polarizer and the other one is called the analyzer as shown in figure 4.4 and 4.5.

4.2. MATERIALS AND METHODS

4.2.1. MATERIALS & EQUIPMENT

Table 4.1: Chemicals used in microfluidic experiments

	Chemical Formula	CAS Number	Vendor
Sodium Oxalate	$Na_2C_2O_4$	62-76-0	Sigma-Aldrich
Calcium Chloride	$CaCl_2$	10043-52-4	Sigma-Aldrich
Ultra pure Water	H_2O	-	Elga
Hydrofluoroether	3-Ethoxy-1,1,1,2,3,4,4,5,5,6,6,6-dodecafluoro-2-trifluoromethylhexane	297730-93-9	3M
Pico-Surf 1	-	-	Sphere Fluidics
Sodium Hydroxide	$NaOH$	1310-73-2	Sigma-Aldrich
Hydrogen Chloride	HCl	7647-01-0	Sigma-Aldrich
Glycine	$C_2H_5NO_2$	1310-73-2	Sigma-Aldrich
Magnesium Chloride	Cl_2Mg	7786-30-3	Sigma-Aldrich
Sodium Acetate	CH_3COONa	127-09-3	Sigma-Aldrich
Acetic Acid	$c(CH_3COOH)$	64-19-7	Sigma-Aldrich

Table 4.2: Equipment used in microfluidic experiments

Equipment	Equipment Name	Brand
Scale	-	Mettler Toledo
Sonicator	2510 Ultrasonic Cleaner	Branson
Heating plate	-	iSL
Microscope	Ti-eclipse	Nikon
pressure pump	MFCS - EZ	Fluigent

4.2.2. SOLUTION PREPARATION

To prepare the solutions the same equation 2.22 is used. In table 4.8 the amounts of calcium chloride and sodium oxalate used is tabulated. These amounts are dissolved into 100 ml of ultra pure water. As was done before with the lab scale experiments, in section 2.2.2. These solutions are made new every experiment to rule out contamination.

Table 4.3: Amount of chemical needed to prepare the supersaturated solutions for microfluidic experiments

Supersaturation ratio	Calcium chloride (mg/100ml solution)	Calcium chloride (mmol/L)	Sodium oxalate (g/100ml solution)	Sodium oxalate (mmol/L)
10	3.04	0.27	3.67	0.27
15	4.56	0.41	5.51	0.41
20	6.08	0.55	7.34	0.55
30	9.12	0.82	11.01	0.82
40	12.16	0.11	14.68	0.11

For the preparation of the solution used in the pH experiment, a large quantity of buffer is made beforehand. To make these buffers a glycine solution and sodium acetate solution were made. These buffer solutions were adjusted to the pH needed by adding a acid or basic solution. The amounts of chemical used are tabulated in table 4.4.

Table 4.4: Amount of chemicals needed to prepare the buffer solutions for pH experiments

pH	x ml 0.2M-NaOAc	y ml 0.2M-HOAc	a ml 0.2M-Glycin	b ml 0.2M-HC	c ml 0.2M-NaOH	d ml ultra pure water
3.6	-	-	25	2.5	-	72.5
6.0	92.0	8.0	-	-	-	-
8.6	-	-	25	-	2.0	73.0

After making the buffer solutions with the above mentioned ratios [42], the supersaturated solutions are made by taking the same amounts of calcium chloride and sodium oxalate for supersaturation ratio 30 described in table 4.3. The only difference is the substitution of ultra pure water with buffer solution.

For the magnesium inhibitor experiments part of the ultra pure water is substituted with magnesium chloride solution according to table 4.5.

Table 4.5: Amount of magnesium chloride needed to prepare the supersaturated solutions for inhibitor experiments

Magnesium chloride (mmol/L)	Magnesium chloride (ml)	Calcium chloride (mg/100ml solution)	Ultra pure water (ml)
0	0	9.12	100
0.01	0.002	9.12	99.998
0.1	0.02	9.12	99.98
0.175	0.035	9.12	99.965
0.2	0.04	9.12	99.96
0.25	0.05	9.12	99.95

Osteopontin is a compound that binds with calcium which prevents stone formation and comes in small quantities of 50μg. This is the reason why the solution is made just enough to run the experiment once at different concentrations. First 50 μg of osteopontin is dissolved into 6.25 ml of ultra pure water, this will give a 6.25 ml stock solution with a concentration of 8 μg/ml. After making the osteopontin stock solution, it should be stored in the fridge. Now the calcium chloride and sodium oxalate solutions should be made. The calcium chloride solution can be made according to supersaturation ratio 30 in table 4.3. The sodium oxalate solution deviates from this table and should be made according to table 4.6 and 4.7.

Table 4.6: Amount of sodium oxalate needed to prepare the supersaturated solutions for osteopontin inhibitor experiments

Osteopontin ($\mu g/ml$)	Sodium oxalate (mg)	Ultra pure water (ml)
2	15.9	100
4	24.2	100
6	47.7	100

After making the solutions, the osteopontin can be mixed with the sodium chloride solution according to table 4.7. This should be done directly inside the reservoir of the pressure pumps to avoid wastage of the

osteopontin. The concentration of inhibitors used were decided with taking into account Tsuji Hidenori work [43].

Table 4.7: Amount of stock solution needed to prepare the supersaturated solutions for inhibitor experiments

Osteopontin ($\mu g/ml$)	**Osteopontin stock solution (ml)**	**Sodium oxalate stock solution (ml)**
2	0.75	3.25
4	1.5	1.5
6	2.25	0.75

4.2.3. OIL PREPARATION

The oil that is used for the microfluidic experiments as a continuous phase consist of two components, oil and surfactant. Different kinds of oils have been tested and HFE oil has been chosen in the end. This decision was made due to the fact that its an inert oil and its compatibility with PDMS, this means that the oil will not get absorbed into the pores of the microfluidic device. The surfactant that needs to be added to it was recommended by the transport phenomena department where they use it for the same purpose of creating droplets in microfluidic devices.

The surfactant is a pre-mixed solution containing HFE oil and 5% V/V pico surfactant. This solution is further diluted by adding HFE oil until it has reached a surfactant concentration of 0.5% V/V. This mixture needs to be made new every time or stored air tight, because HFE evaporates at room temperature.

4.2.4. PRESSURE PUMPS

To use the pressure pump the reservoirs needs to filled up first. This is done by injecting the solution through the tubing into the reservoir. The reason behind this is to fill up the tubing at the same time to avoid getting air into the system. After filling up the tubing and the reservoir with around 1.5 ml of solution, the pressure pump can be started. First the pressure valve should be opened, after that the pressure divider can be turned on at the back of the device and started with the play button on the front. When the pressure pump is ready for use, the pressure will be set to around 73 mbar for all the 3 inlets with the AIO software. In figure 4.6 a schematic is given of the full setup of the experiment.

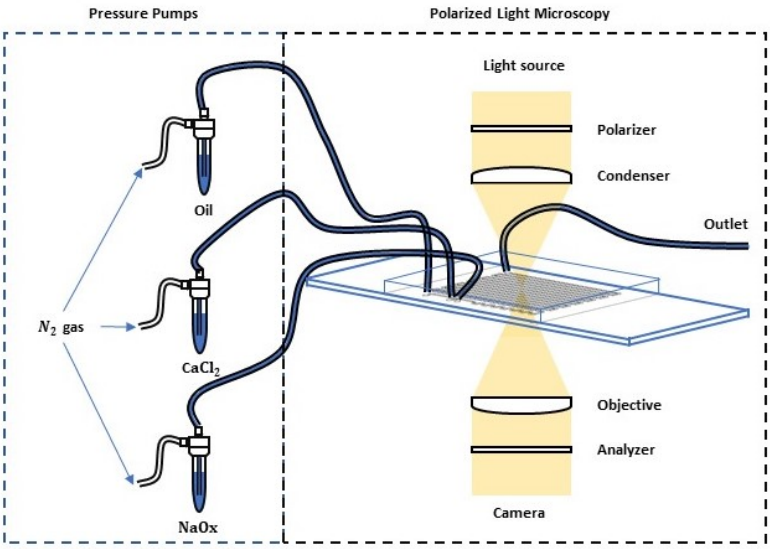

Figure 4.6: Schematic of the pressure pump setup

4.2.5. POLARIZED LIGHT MICROSCOPY

For these experiments polarized light microscopy is used. To set this up a filter has to be put between the device and the light source and the analyzer filtercube needs to be selected. To know what polarisation angle is required a small sample with COM crystal is placed under the microscope to find this, the angle found in the case of COM was 0. In figure 4.7 the process of crystallization under polarized light is illustrated.

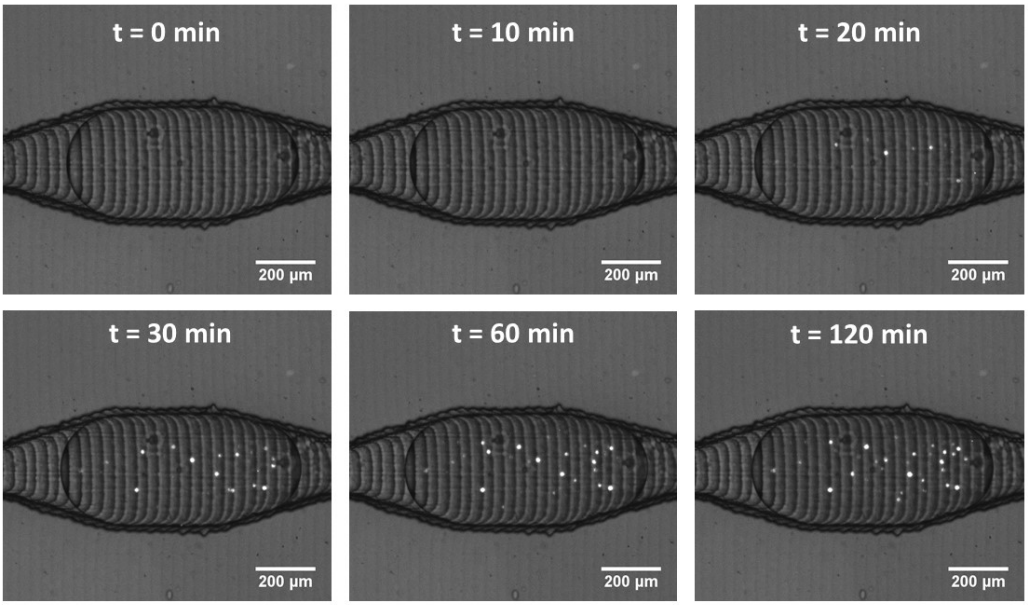

Figure 4.7: Time lapse of crystal formation inside a droplet under polarized light microscopy

4.3. RESULTS & DISCUSSION

4.3.1. DIMENSIONLESS NUMBERS

As mentioned in paragraph 4.1.1, there are a couple of dimensionless numbers that are important when working with microfluidics. In this paragraph the dimensionless numbers will be presented for the microfluidic system used for all the experiments in this chapter.

The first dimensionless number that was mentioned in paragraph 4.1.1 was the Reynolds number. This number gives the relation between inertial forces and the viscous forces. Using equation 4.1 the Reynolds number was calculated and was found to be 2.26, which indicates that the flow inside the microfluidic device is laminar.

The second dimensionless number is the Capillary number. Which was determined to be $2.99x10^{-4}$ using equation 4.2. This means that the interfacial forces is dominating the viscous forces.

The Bond number was calculated with equation 4.3 and was found to be $5.95x10^{-2}$. This means that the gravitational forces are being dominated by the interfacial forces. This helps with maintaining a thin film around the droplet throughout the experiment.

The last dimensionless number is the Weber number, which give the relation between inertial forces and interfacial forces. The Weber number is $6.75x10^{-}4$, this means that the interfacial forces are dominating the inertial forces.

4.3.2. INDUCTION TIME AT DIFFERENT SUPERSATURATION

In the figure 4.8 the cumulative probability distribution is plotted against the detection time. In this graph the Weibull model is used as fitting function, as has been decided in chapter two. Supersaturation ratio 10 shows no crystals over the time period of 350 min, whereas the supersaturation ratio of 40 show crystals after the 1.5 min needed to make the first image. This means that the maximum limit of supersaturation ratio that can be tested is 40. Higher ratios can not be used due to the limitations of the method and microscope. The microscope takes up to 1.5 minutes to make a full image of the microfluidic device, this means that it is not possible to make an image before the crystallization happens. For the low supersaturation ratio 10 it is possible to obtain these data. The running time of 350 min can be extended until the droplets starts crystallizing. For supersaturation ratio 15 the first droplets were crystals can be detected was around 50 min after starting the experiment. Supersaturation ratio 20 showed crystals after 12 minutes and 30 starts from 6 minutes.

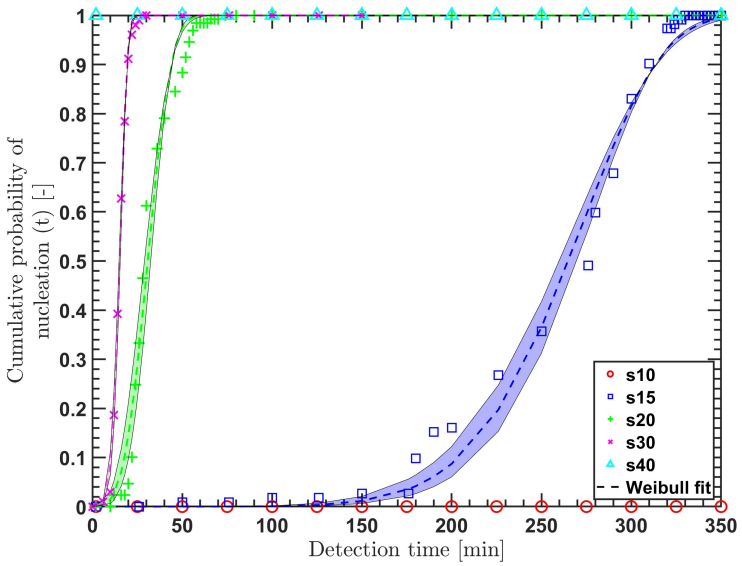

Figure 4.8: Probability curves at different supersaturation ratio fitted with the Weibull model

The parameters obtained from the Weibull model are tabulated in table 4.8 below. The k values for all the supersaturation ratios are, just as the ones from the lab scale experiments, above one. This indicates that there is a increasing nucleation rate. For supersaturation ratio 10 and 40 no parameter has been found, because no data could be extracted that can be used for curve fitting.

Table 4.8: Parameters k and τ from Weibull model fitted into the probability distribution at different supersaturation ratio

Supersaturation	k	**95% confidence interval**	τ **(min)**	**95% confidence interval**
10	-	-	-	-
15	6.50	5.66, 7.34	275.69	271.19, 280.19
20	3.00	2.62, 3.39	33.67	32.45, 34.90
30	3.80	3.13, 4.47	15.74	15.22, 16.26
40	-	-	-	-

The results obtained from the supersaturation ratio experiments are all according to expectation, were the supersaturation ratio increases the median nucleation time will decrease. Also as expected, the nucleation rate will increase with an increase in supersaturation ratio.

Table 4.9: The calculated median nucleation time and nucleation rate for the 3 different supersaturation ratios

Supersaturation ratio	**Median nucleation time(min)**	**J** $(nuclei\ s^{-1}\ L^{-1})$
15	293.48	1014.10
20	38.10	8100.83
30	17.60	16731.67

After calculating J and t_{med}, the kinetic and thermodynamic parameters can be determined in the same way as done in chapter 2. The linear curve in figure 4.9 shows that The kinetic parameter will be -42.26 and the Thermodynamic parameter will be 21.22.

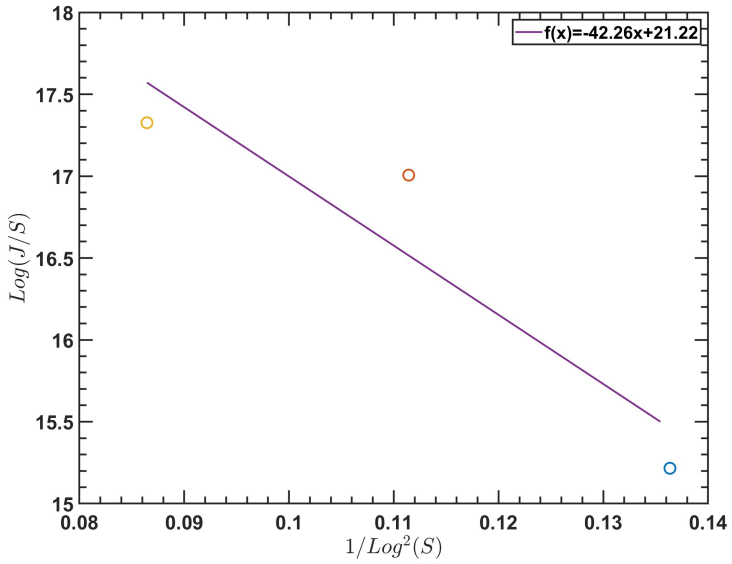

Figure 4.9: Logarithmic plot of J/S versus S to obtain the kinetic and thermodynamic parameters

4.3.3. pH DEPENDENT INDUCTION TIME

For the pH dependency experiments, three pH values were chosen. These pH values are 6.0 which is the average value inside the kidney. Acidic pH 3.6 which can be the result of ingesting acidic foods such as products with high sugar contents or medical conditions such as diabetes. Basic pH 8.6 in the kidney can be caused by nuts or medical conditions such as infections or kidney stones [44].

In figure 4.10 the results have been plotted with the Weibull model. This figure shows that crystals can be detected for pH 3.6 and 8.6 after 30 and 10 min respectively. For pH 6.0 no crystals were found after running the experiment for 700 min. The reason for this can be due to the fact that at pH 6.0 the solubility is higher than at 3.6 and 8.6. This is according to the results obtained by member of the same department F. Ibis. The higher solubility will decrease the supersaturation ratio according to equation 2.2, which will lead to an increase in induction time and decrease in nucleation rate.

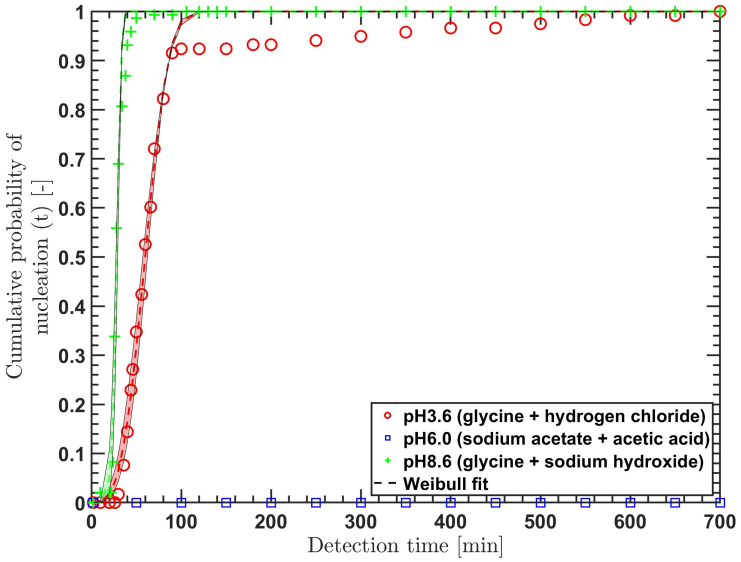

Figure 4.10: Probability curves at different pH fitted with the Weibull model

The k values from the pH dependent experiments gives the same result as previous experiments, which is above one. The time scale value of pH 3.6 is higher than that of 8.6. This can be explained by looking at the solubility curve in appendix C, made by past member of the departmend P. dhand [45]. In this figure, the solubility at pH 3.6 is higher that that of 8.6. This means that the supersaturation ratio of 3.6 will be lower that that of 8.6.

Table 4.10: Parameters k and τ from Weibull model fitted into the probability distribution at different pH

pH	k	**95% confidence interval**	τ **(min)**	**95% confidence interval**
3.6	2.94	2.61, 3.27	65.47	63.54, 67.40
6.0	-	-	-	-
8.6	7.13	5.66, 8.61	29.68	28.99, 30.38

4.3.4. INHIBITORS

MAGNESIUM

The first inhibitor that was tested is magnesium which is an inorganic inhibitor. The mechanism behind this inhibition works as follows, the magnesium ions forms magnesium oxalate together with the oxalate ions present in the solution. This will reduce the supersaturation ratio of oxalate which is needed to nucleate [46]. The first two concentrations that were tested were the lowest one 0.01 mmol/l and the highest one 0.25 mmol/L. This will give a range in were magnesium starts taking effect. The second batch of experiments were performed with 0.1 and 0.2 mmol/L, the results gave a indication that the critical concentration lies somewhere between those two concentrations. As last the concentration of 0.175 mmol/L has been chosen to be tested.

The results in figure 4.11 shows similair curves for concentrations 0, 0.01 and 0.1 mmol/L. From concentration 0.175 onward the curves starts shifting. The concentration of 0.2 mmol/L was the limit of this experimental

protocol where the running time was 100 min. The figure shows that for concentration 0.25 mmol/L there were no crystals found after completing the run of 100 min.

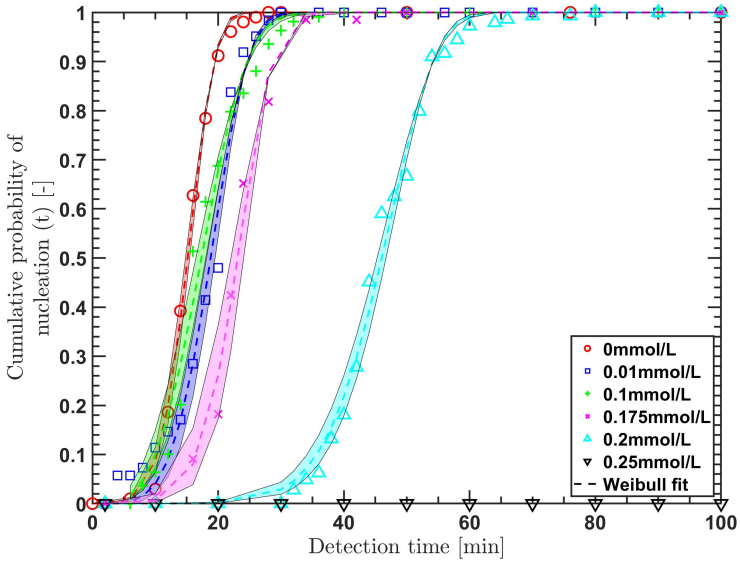

Figure 4.11: Probability curves at different Magnesium concentrations fitted with the Weibull model

As expected following the previous results, the k value is above one which indicates that the nucleation rate is increasing even with inhibitors present. In table 4.11 The time scale values starts showing and significant increase starting from concentration 0.175 mmol/L.

Table 4.11: Parameters k and τ from Weibull model fitted into the probability distribution at different magnesium concentrations

Magnesium concentration (mmol/L)	k	**95% confidence interval**	τ **(min)**	**95% confidence interval**
0	3.80	3.08, 4.52	15.74	15.18, 16.30
0.01	2.62	1.95, 3.29	19.03	17.72, 20.35
0.1	3.10	2.70, 3.50	18.90	19.33, 19.47
0.175	4.53	3.12, 5.93	24.17	23.08, 25.26
0.2	7.39	6.67,8.11	48.36	47.85, 48.86
0.25	-	-	-	-

OSTEOPONTIN

The second inhibitor that was tested is osteopontin which is an organic inhibitor. The mechanism behind this inhibitor is that this protein has the ability to bind calcium, which will decrease the supersaturation ratio. This is not the only effect that osteopontin has on kidney stones. Osteopontin also has effect on the growth and the binding of calcium oxalate crystals to the cells inside the kidney [43]. The three concentrations that have been tested were 2, 4 and 6 μg/ml.

The two higher concentrations did not give any results after running the experiments for more than three hours. This means that the running to of the experiment needs to be extended to obtain crystal detection time data. For osteopontin concentration 2 μg/ml the data showed signs of inhibition.

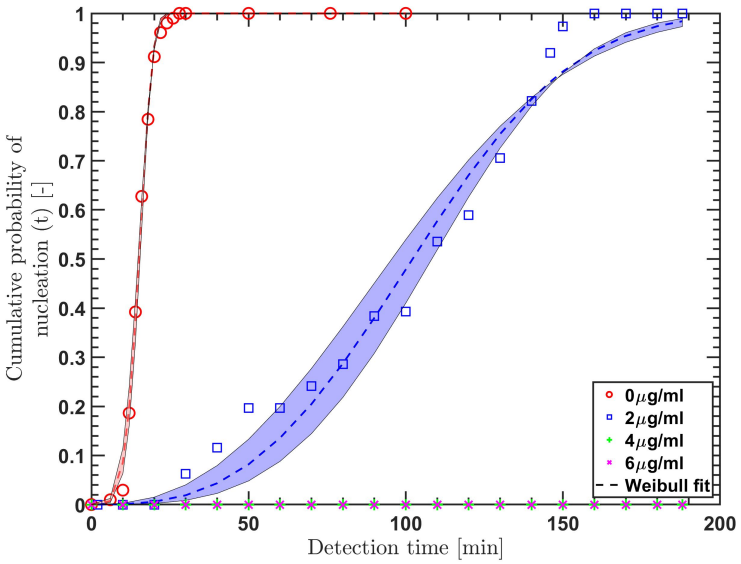

Figure 4.12: Probability curves at different osteopontin concentrations fitted with the Weibull model

The k values for osteopontin inhibition experiment shows that the inhibitor does not influence shape parameter, which means that this is still a nucleation rate increasing process.

Table 4.12: Parameters k and τ from Weibull model fitted into the probability distribution at different osteopontin concentrations

Osteopontin ($\mu g/ml$)	k	**95% confidence interval**	τ **(min)**	**95% confidence interval**
0	4.91	4.43, 5.40	16.34	16.09, 16.58
2	2.93	2.44, 3.42	115.78	110.99, 120.57
4	-	-	-	-
6	-	-	-	-

5

CONCLUSION

5.1. INDUCTION TIME

5.1.1. LABORATORY SCALE

To get more reliable results for lab scale experiments, more data from the FBRM should be obtained. With the amount of results available now, no solid conclusion can be made. The trend of the results do go as expected, when the supersaturation ratio increases the induction time will decrease. The exponential model does not fit well with all the supersaturation ratios. Also induction time values that are not possible were obtained when fitted into the FBRM results. This is the reason why the Weibull model is used for the rest of the experiments.

5.1.2. MICROFLUIDICS

The microfluidic part of this thesis was a were according to expectations. A microfluidic device was designed from scratch and has been optimized for the purpose of this thesis. This device can form droplets out of two solutions, which will undergo reactive crystalization. The droplets can be kept at a fixed location throughout the experiment of at least 6 hours. The obtained results for the induction times with the microfluidic device are also according to expectations, as the supersaturation ratio increases the induction time will decrease and vice versa.

5.1.3. DIFFERENCE BETWEEN THE TWO SCALES

No comparison can be made between the two scales. The lab scale results obtained from the FBRM were not trustworthy. The amount of data obtained were far too low, this will give results that are either wrong or have a big error. The only conclusion that can be made is that using microfluidics will obtain more data in a shorter period of time, which will lead to more accurate results. Another advantage of the microfluidic experiments are the experimental conditions, these will be the same for all the individual droplets. This cannot be done with the lab scale experiments, where the solution has to be made new for every new experiment. The only advantage of the FBRM is that it measures and crystal count automatically, whereas the microfluidic experiment data needs to be processed manually. When counting crystals manually, there is a possibility of introducing a human error.

5.2. INFLUENCE OF PH

The pH experiments shows that the induction time at pH 8.6 and 3.6 are lower than that of 6.0. This is all according to expectation when looking at the solubility result of P. Dhand [45]. When looking back at the supersaturation ratio equation 2.2, the supersaturation ratio is linked to the solubility of the compound. When the solubility increases and the concentration is kept constant, the supersaturation ratio will drop. There is also a chance that the buffer solution is influencing the crystallization at pH 6.0. The reason for this hypothesis is the difference in buffer solution used for pH 3.6/8.6 and pH 6.0.

5.3. INFLUENCE OF INHIBITORS

5.3.1. MAGNESIUM

According to studies of Kulaksizoglu et al. [46] aggregation and nucleation can be inhibited by approximately 70 percent at high concentrations of magnesium. For the Magnesium inhibitor experiments in this thesis, the results shows that starting from a concentration of 0.175 mmol/L the magnesium starts taking effect. Concentrations lower than this critical concentration show little to no effect at all.

5.3.2. OSTEOPONTIN

In the studies of Hidenori et al. [43], the osteopontin concentrations in patients with urolithiasis were investigated. In this research the conclusion has been made that patients with urolithiasis have a lower concentration of osteopontin in their excretion. For the three tested concentration of osteopontin in this thesis, only 2 μg/ml shows crystal formation. The two higher ones shows no crystals at all. This means that the critical concentration lies between 2 and 4 μg/ml.

6

RECOMMENDATION

- To get a more accurate comparison of the supersaturation experiments between lab scale and microfluidics, the lab scale experiment with the FBRM should be repeated. No solid conclusion can be made with the results obtained from the FBRM. This repetition does not need to be for all the supersaturation that has been done in the microfluidic setup. Three supersaturations are more than enough for just a comparison. As this thesis has already concluded that microfluidics are more suited for induction time experiments.
- More experiments are needed at different supersaturations ratios to obtain a more accurate $ln\left(\frac{J}{S}\right)$ versus $ln^2(S)$ curve. With 3 data points are not enough to make a solid conclusion if the curve is linear. If this curve is linear then the nucleation follows the classical nucleation theory.
- A better protocol for semi-curing of the glass slides is needed. By improving this protocol, the success rate of making usable microfluidic devices will increase drastically.
- The fabrication of the chips should be done inside a dust free environment. This will decrease the impurities that light up under the polarized light microscopy, which will make analyzing the pictures a lot easier.
- A code needs be generated for automation of the image analysis. This will not only reduce the workload but also increase the accuracy of the obtained results.
- To get an even better understanding of the formation of kidney stones, the design of the moulds can be changed to implement various structures that are present inside the human kidney.
- Not only the structures inside the kidney can be mimicked but also the physiological condition. This can be achieved by for example introducing artificial urine or other bodily substances.
- The experiments are performed at room temperature, but the temperature of the human body is at 37 degrees Celsius. This can be achieved by either designing a device that can heat up the chip or finding a commercially available device that does this.
- More supersaturation ratio experiments needs to be performed to check if the Weibull model is indeed the best choice to fit the cumulative probability distribution.
- A wide range buffer solution needs to be found that will not react with either calcium or oxalate. In this thesis two different buffer solutions were used, which gave favorable results. But it is uncertain if this result is due to the fact that a different buffer solution is used or by the increase in solubility at pH 6.0.

BIBLIOGRAPHY

[1] T. Knoll, *Epidemiology , Pathogenesis , and Pathophysiology of Urolithiasis,* European Urology Supplements **9**, 802–806 (2010).

[2] A. T. Taylor, *Reference Values for Renal Size Obtained From MAG3 Scintigraphy,* Clin Nucl Med. **38**, 13–17 (2014).

[3] B. Blausen, *Medical gallery of Blausen Medical 2014,* **1** (2014), 10.15347/wjm/2014.010.

[4] T. Alelign, *Kidney Stone Disease : An Update on Current Concepts,* **2018** (2018), 10.1155/2018/3068365.

[5] A. P. Evan, *Physiopathology and etiology of stone formation in the kidney and the urinary tract,* , 831–841 (2010).

[6] F. U. Grases, *Biopathological crystallization : a general view about the mechanisms of renal stone formation,* , 169–194 (1998).

[7] V. Romero, H. Akpinar, and D. G. Assimos, *Kidney Stones : A Global Picture of Prevalence , Incidence , and Associated Risk Factors Kidney Stones : A Global Perspective,* **12**, 86–96 (2010).

[8] H. Han, A. M. Segal, J. L. Seifter, and J. T. Dwyer, *Nutritional Management of Kidney Stones (Nephrolithiasis),* , 137–152 (2015).

[9] L. H. Smith, W. G. Robertson, and B. Finlayson, *Urolithiasis - Clinical and Basic Research* (1981).

[10] X. Sheng, M. D. Ward, and J. A. Wesson, *Crystal Surface Adhesion Explains the Pathological Activity of Calcium Oxalate Hydrates in Kidney Stone Formation,* , 1904–1908 (2005).

[11] N. L. Miller and J. E. Lingeman, *Management of kidney stones,* BMJ **334**, 468–472 (2007).

[12] A. Effects, *Conferences and Reviews Extracorporeal Shock Wave Lithotripsy of Urinary Calculi Theory , Efficacy , and Adverse Effects,* , 65–69 (1990).

[13] Urology Care Foundation, *Kidney Stones : A Patient Guide,* .

[14] H. Sekar, S. Krishnamoorthy, N. Kumaresan, and V. Ramanan, *Supracostal Punctures for PCNL : Factors that Predict Safety , Success and Stone Free Rate in Stag Horn and Non-Stag Horn Stones : A Single Centre Experience and Review of Literature,* , 17–21 (2016).

[15] D. Kashchiev and G. M. V. Rosmalen, *Review : Nucleation in solutions revisited Driving force,* **574**, 555–574 (2003).

[16] K. H.J.M., v. R. G.M., and t. H. J.H., *Basic Process Design for Crystallization Processes,* .

[17] A. Malthe sørenssen, *Chemical potential and Gibbs Distribution* (2013).

[18] W. D. Callister and D. G. Rethwisch, *Materials Science and Engineering an Introduction,* 8th ed. (2009).

[19] S. Jiang and J. H. ter Horst, *Crystal Nucleation Rates from Probability Distributions of Induction Times,* Crystal Growth & Design **11**, 256–261 (2011).

[20] V. N. Ratkalkar and J. G. Kleinman, *Mechanisms of Stone Formation,* **9**, 187–197 (2012).

[21] J. H. T. Horst, *Measuring Induction Times and Crystal Nucleation Rates Measuring induction times and crystal nucleation rates,* (2015), 10.1039/C4FD00230J.

[22] R. P. Sear, *supersaturation : experimental data and models,* , 6506–6522 (2014).

[23] Mettler Toledo, *iC FBRM Documentation Portfolio,* (2015).

[24] B. Shi, S. A, L.-Y. B, X. Lv, H.-S. D, H.-H. A, W. Wang, D. A, and J. A, *Viscosity investigation of natural gas hydrate slurries with anti-agglomerants additives,* Fuel **185** (2016), 10.1016/j.fuel.2016.07.113.

[25] H. Mccomas, L. Huggins, and I. Part, *The Solubility of Calcium Oxalate Monohydrate in Pure Water and Various Neutral Calcium Oxalate,* **459** (1933), 10.1021/ja01264a060.

[26] J.-h. Jeon, S. Khan, L. Gower, and Y. Rabinovich, *A study of primary nucleation of calcium oxalate monohydrate : I-Effect of supersaturation,* **221**, 214–221 (2004).

[27] M. D. Schneider, *Induction time analysis of the precipitation of calcium oxalate monohydrate using focused beam reflectance measurement technology*, Bsc thesis, University of Technology Delft (2018).

[28] B. Zhang, K. Kowsari, A. Serjouei, M. L. Dunn, and Q. Ge, *dimensional printing,* 10.1038/s41467-018-04292-8.

[29] Roland, *3D Digital Fabrication,* .

[30] Envisiontec, *Operation Manual Micro Hi-res Plus,* , 1–8 (2017).

[31] Dentalfarm, *Operation Manual Photopol Curing Unit,* , 1–2 (2017).

[32] P. Garstecki, M. J. Fuerstman, H. A. Stone, and G. M. Whitesides, *Formation of droplets and bubbles in a microfluidic T-junction—scaling and mechanism of break-up,* Lab Chip **6**, 437–446 (2006).

[33] J. M. Ottino, *The kinematics of mixing : stretching , chaos , and transport,* .

[34] P. V. Danckwerts, *The definition and measurement of some characteristics of mixtures,* Applied Scientific Research, Section A **3**, 279–296 (1952).

[35] O. Altenburg, *Influence of mixing and surfactants in microfluidic induction time measurements Influence of mixing and surfactants in microfluidic induction time measurements*, Ph.D. thesis.

[36] P. van Tooren, *Nucleation Rate Behaviour in Induction Time Experiments & Increasing Droplet Carry Capacity in Microfluidic Systems*, Bsc thesis, University of Technology Delft (2018).

[37] C. House, *Transition from squeezing to dripping in a microfluidic T-shaped junction,* **595**, 141–161 (2008).

[38] W. Han and X. Chen, *New insights into generation of highly controllable monodisperse high-throughput microdroplets in a T-junction microchannel with step structure,* Journal of Dispersion Science and Technology **0**, 1–12 (2019).

[39] H. Gu, M. H. G. Duits, and F. Mugele, *Droplets Formation and Merging in Two-Phase Flow Microfluidics,* , 2572–2597 (2011).

[40] M. Baudoin, *Microfluidics,* .

[41] C.-a. Kieffer, S. Ritty, T. Boudot, N. Petit, J. Weber, and A. L. E. Nel, *FLOW RATE CONTROL PRESSURE REGULATION FEATURES AND BENEFITS OF THE NEW FLOW-RATE ALGORITHM,* , 1–4.

[42] R. M. C. Dawson, *Data for Biochemical Research* (1986).

[43] H. Tsuji, U. Tohru, U. Hirotsugu, I. Masanori, H. Yuji, and K. Takashi, *Urinary concentration of osteopontin and association with urinary supersaturation and crystal formation,* International Journal of Urology **14**, 630–634 (2007).

[44] R. Nall, *What is the normal pH range for urine?* (2018).

[45] P. Dhand, *Effect of pH on the Solubility of Calcium Oxalate Monohydrate Crystals and Lab-on-a-Chip Technology for Hypercalciuria*, Msc thesis, University of Technology Delft (2019).

[46] S. Kulaksizoglu, M. Sofikerim, and C. Cevik, *Impact of various modifiers on calcium oxalate crystallization,* , 214–218 (2007).

A

MATLAB CODE

```
clc
close all
clear

data = xlsread('C:\Users\Tsun wang Yu\Downloads\Test.xlsx','Sheet2');

PB1 = data(:,1:2);
PB1(all(isnan(PB1),2),:)= [];
PB2 = data(:,4:5);
PB2(all(isnan(PB2),2),:)= [];
PB3 = data(:,7:8);
PB3(all(isnan(PB3),2),:)= [];
PB4 = data(:,10:11);
PB4(all(isnan(PB4),2),:)= [];
PB5 = data(:,13:14);
PB5(all(isnan(PB5),2),:)= [];

x0 = [1 10];

F = @(c,xdata) 1-exp(-(xdata/c(2)).^c(1));
% F = @(c,xdata) 1-exp(-(xdata-c(1))/c(2));


x1 = PB1(:,1);
x1 = transpose(x1);

x2 = PB2(:,1);
x2 = transpose(x2);

x3 = PB3(:,1);
x3 = transpose(x3);

x4 = PB4(:,1);
x4 = transpose(x4);

x5 = PB5(:,1);
x5 = transpose(x5);

[c2, resnorm2,residual2,exitflaf2, out2,lambda2,jacobian2] =
 lsqcurvefit(F,x0,PB2(:,1),PB2(:,2));
conf = nlparci(c2,residual2,'jacobian',jacobian2); %noice func
resul2 = [transpose(c2), conf];

PB22 = F(c2,PB2(:,1));

[c3, resnorm3,residual3,exitflaf3, out3,lambda3,jacobian3] =
 lsqcurvefit(F,x0,PB3(:,1),PB3(:,2));
conf = nlparci(c3,residual3,'jacobian',jacobian3); %noice func
resul3 = [transpose(c3), conf];

PB33 = F(c3,PB3(:,1));
```

```
[c4, resnorm4,residual4,exitflaf4, out4,lambda4,jacobian4] =
 lsqcurvefit(F,x0,PB4(:,1),PB4(:,2));
conf = nlparci(c4,residual4,'jacobian',jacobian4); %noice func
resul4 = [transpose(c4), conf];

PB44 = F(c4,PB4(:,1));

figure(1)
L(1) = scatter(PB1(:,1),PB1(:,2),150,'ro','linewidth',2);
hold on

L(2) = scatter(PB2(:,1),PB2(:,2),150,'bs','linewidth',2);
hold on
PBg3 = plot(PB2(:,1), PB22(:,1),'b--','LineWidth',2);
set(get(get(PBg3,'Annotation'),'LegendInformation'),'IconDisplayStyle','off');
hold on

a2 = [resul2(1,2), resul2(2,2)];
PB222 = F(a2, PB2(:,1));
PB222 = transpose(PB222);

b2= [resul2(1,3), resul2(2,3)];
PB2222 = F(b2, PB2(:,1));
PB2222 = transpose(PB2222);

x22 = [x2, fliplr(x2)];
inBetween2 = [PB222, fliplr(PB2222)];
PBg4 = fill(x22, inBetween2, 'b');
set(get(get(PBg4,'Annotation'),'LegendInformation'),'IconDisplayStyle','off');
alpha(.3);

L(3) = scatter(PB3(:,1),PB3(:,2),150,'g+','linewidth',2);
hold on
PBg5 = plot(PB3(:,1), PB33(:,1),'g--','LineWidth',2);
set(get(get(PBg5,'Annotation'),'LegendInformation'),'IconDisplayStyle','off');
hold on

a3 = [resul3(1,2), resul3(2,2)];
PB333 = F(a3, PB3(:,1));
PB333 = transpose(PB333);

b3= [resul3(1,3), resul3(2,3)];
PB3333 = F(b3, PB3(:,1));
PB3333 = transpose(PB3333);

x33 = [x3, fliplr(x3)];
inBetween3 = [PB333, fliplr(PB3333)];
PBg6 = fill(x33, inBetween3, 'g');
set(get(get(PBg6,'Annotation'),'LegendInformation'),'IconDisplayStyle','off');
alpha(.3);

L(4) = scatter(PB4(:,1),PB4(:,2),150,'mx','linewidth',2);
hold on
L(6:7) = plot(PB4(:,1), PB44(:,1),'m--',nan,nan,'k--','LineWidth',2);
```

```
hold on

a4 = [resul4(1,2), resul4(2,2)];
PB444 = F(a4, PB4(:,1));
PB444 = transpose(PB444);

b4= [resul4(1,3), resul4(2,3)];
PB4444 = F(b4, PB4(:,1));
PB4444 = transpose(PB4444);

x44 = [x4, fliplr(x4)];
inBetween4 = [PB444, fliplr(PB4444)];
L(8:9) = fill(x44, inBetween4, 'm',x44,inBetween4,'w');
alpha(.3);

L(5) = scatter(PB5(:,1),PB5(:,2),150,'c^','linewidth',2);

xlabel('Detection time [min]','Interpreter','latex','FontSize',48);
ylabel(['Cumulative probability of' newline 'nucleation (t)
 [-]'], 'Interpreter','latex','FontSize',48);
ylim([0 1]);
legend(L([1,2,3,4,5,7]),'s10','s15','s20','s30','s40','Weibull
 fit','location','southeast');

set(gca, ...
'FontSize',22,...
'FontWeight','bold',...
'Box'         , 'on'     , ...
  'TickDir'     , 'in'     , ...
  'TickLength'  , [.02 .02] , ...
  'XMinorTick'  , 'on'      , ...
  'YGrid'       , 'off'      , ...
  'YMinorTick'  , 'on'      , ...
  'XGrid'       , 'off'      , ...
  'LineWidth'   , 2         );

set(gcf, 'Position', [1, 1, 1200, 895]);
set(gcf,'color','w');
```

Published with MATLAB® R2018a

B

FLOW RATE CALCULATIONS

In table B.1 constants that were used in the dimensionless number calculations are tabulated. Table B.2 shows the amount of mass coming out of the microfluidic system over a time period of 10 min. Using these values the fractions of oil and solutions has been calculated, which were used to calculate the average density, viscosity and velocity. These three average values were needed to calculate the dimensionless numbers.

Table B.1: Constants used for flow rate calculations

ρ_{oil}	1614 g/L
ρ_{sol}	1000 g/L
μ_{oil}	$1.24x10^{-3}$ kg/m.s
μ_{sol}	$8.90x10^{-4}$ kg/m.s
γ_{oil}	$1.62x10^{-2}$ N/m
R_{oil}	$6.33x10^{10}$
R_{sol}	$6.33x10^{10}$

Table B.2: Flow rate data used for dimensionless number calculation

Time (min)	**Mass (g)**	**Q_oil (L/s)**	**Q_sol (L/s)**	**x_oil**	**x_sol**	**Q_out (L/s)**
1	0.0285	7.83E-06	7.93E-06	4.43E-01	5.57E-01	3.73E-07
2.1	0.0608	1.67E-05	1.69E-05	4.43E-01	5.57E-01	3.79E-07
3	0.0843	2.32E-05	2.35E-05	4.43E-01	5.57E-01	3.68E-07
4.1	0.1144	3.14E-05	3.18E-05	4.43E-01	5.57E-01	3.66E-07
5	0.1391	3.82E-05	3.87E-05	4.43E-01	5.57E-01	3.64E-07
6	0.169	4.64E-05	4.70E-05	4.43E-01	5.57E-01	3.69E-07
7	0.198	5.44E-05	5.51E-05	4.43E-01	5.57E-01	3.71E-07
8.1	0.2296	6.31E-05	6.39E-05	4.43E-01	5.57E-01	3.72E-07
9	0.2565	7.05E-05	7.14E-05	4.43E-01	5.57E-01	3.73E-07
10	0.285	7.83E-05	7.93E-05	4.43E-01	5.57E-01	3.73E-07

C

SOLUBILITY CURVE

Figure C.1 shows a solubility curve as function of pH, which was made by past member of the department P. Dhand [45]. This figure shows peak in solubility at a pH 5.8. The solubility increases initially with a increase in pH, but decreases steeply after pH 5.8.

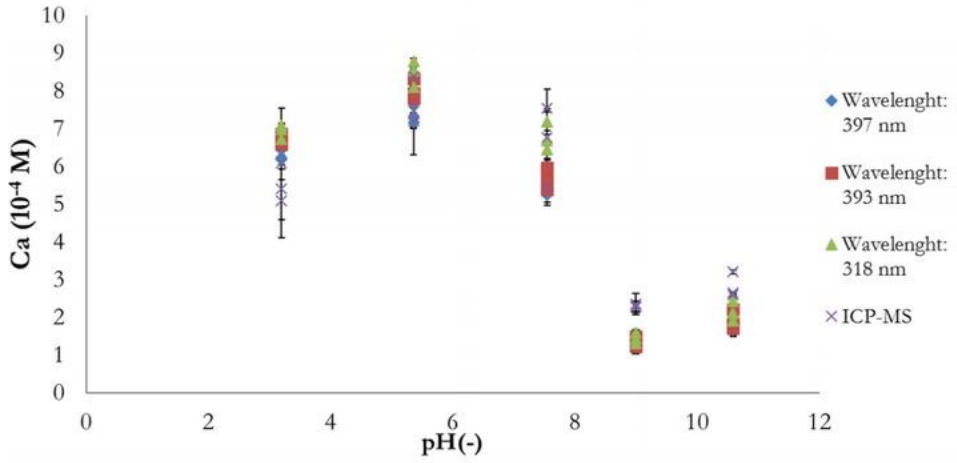

Figure C.1: Solubility of calcium oxalate at different pH